A TRIDENT SCHOLAR PROJECT REPORT

NO. 516

Structural and Magnetic Properties of Iron-Palladium and Iron-Nickel Nanoparticle Biocomposites

by

Midshipman 1/C Matthew J. Fox, USN

UNITED STATES NAVAL ACADEMY
ANNAPOLIS, MARYLAND

USNA-1531-2

REPORT DOCUMENTATION PAGE

Form Approved
OMB No. 0704-0188

1. REPORT DATE *(DD-MM-YYYY)*
5-16-22

2. REPORT TYPE

3. DATES COVERED *(From - To)*

4. TITLE AND SUBTITLE
Structural and Magnetic Properties of Iron-Palladium and Iron-Nickel Nanoparticle Biocomposites

5a. CONTRACT NUMBER

5b. GRANT NUMBER

5c. PROGRAM ELEMENT NUMBER

6. AUTHOR(S)
Matthew J. Fox

5d. PROJECT NUMBER

5e. TASK NUMBER

5f. WORK UNIT NUMBER

7. PERFORMING ORGANIZATION NAME(S) AND ADDRESS(ES)

8. PERFORMING ORGANIZATION REPORT NUMBER

9. SPONSORING / MONITORING AGENCY NAME(S) AND ADDRESS(ES)
U.S. Naval Academy
Annapolis, MD 21402

10. SPONSOR/MONITOR'S ACRONYM(S)

11. SPONSOR/MONITOR'S REPORT NUMBER(S)
Trident Scholar Report no. 516 (2022)

12. DISTRIBUTION / AVAILABILITY STATEMENT

This document has been approved for public release; its distribution is UNLIMITED.

13. SUPPLEMENTARY NOTES

14. ABSTRACT

Biocomposites containing magnetic nanoparticles have the potential to combine the unique, tunable properties of nanoparticles with the strong mechanical and environmentally sustainable properties of natural fibers like cellulose. Recently, a method to synthesize Fe-Pd nanoparticles in cellulose has been developed. This study presents a detailed investigation on how magnetic properties of Fe-Pd nanoparticles are affected by increasing the metal load at a fixed atomic composition. An analysis of their magnetic response in static and dynamic magnetic fields indicates a polydisperse ensemble of nanoparticles with up to four distributions of blocking temperatures. In addition to the Fe-Pd studies, novel Fe-Ni nanoparticle biocomposites are presented for the first time. A unique energetic event was observed during the nitrogen reduction in Fe-Ni composites with low Fe-content. During this event, the cellulose matrix is degraded, an ensemble of Ni-Fe magnetic nanoparticles is formed, and the materials appear to store hydride. For samples for which no energetic event occurs, limited nanoparticle growth and weak magnetic properties are observed. The introduction of Fe into the Ni matrix appears to cause increased magnetic disorder. Both systems have been developed and characterized with the goal of creating magnetically active nanoparticle biocomposites for potential applications in electromagnetic shielding.

15. SUBJECT TERMS
Magnetic nanoparticles, AC magnetic susceptibility, biocomposites, electromagnetic shielding, iron-nickel, iron-palladium

16. SECURITY CLASSIFICATION OF:			**17. LIMITATION OF ABSTRACT**	**18. NUMBER OF PAGES**	**19a. NAME OF RESPONSIBLE PERSON**
a. REPORT	**b. ABSTRACT**	**c. THIS PAGE**		49	**19b. TELEPHONE NUMBER** *(include area code)*

U.S.N.A. --- Trident Scholar project report; no. 516 (2022)

STRUCTURAL AND MAGNETIC PROPERTIES OF IRON-PALLADIUM AND IRON-NICKEL NANOPARTICLE BIOCOMPOSITES

by

Midshipman 1/C Matthew J. Fox
United States Naval Academy
Annapolis, Maryland

(signature)

Certification of Advisors' Approval

Professor Elena Cimpoiasu
Physics Department

(signature)

(date)

CDR David P. Durkin, USN
Chemistry Department

(signature)

(date)

Acceptance for the Trident Scholar Committee

Professor Maria J. Schroeder
Associate Director of Midshipman Research

(signature)

(date)

USNA-1531-2

1. Abstract

Biocomposites containing magnetic nanoparticles have the potential to combine the unique, tunable properties of nanoparticles with the strong mechanical and environmentally sustainable properties of natural fibers like cellulose. Materials derived from biocomposites can be used for a broad variety of civilian and military applications including electromagnetic shielding, thermoelectrics, functional textiles, and water filtration. Many recent studies have focused on magnetic nanoparticles because of the unique properties that emerge when the size of particle reaches the nanoscale. Recently, a method to synthesize Fe-Pd nanoparticles in cellulose has been developed. This study presents a detailed investigation on how magnetic properties of Fe-Pd nanoparticles are affected by increasing the metal load at a fixed atomic composition. An analysis of their magnetic response in static and dynamic magnetic fields indicates a polydisperse ensemble of nanoparticles with up to four distributions of blocking temperatures. Each distribution of blocking temperatures corresponds to a distinct group of particles. Peak dependence on frequency, field, and load was analyzed for each group of nanoparticles. In addition to the Fe-Pd studies, novel Fe-Ni nanoparticle biocomposites are presented for the first time. A unique energetic event during the N_2 reduction at 120 °C has been observed in samples with ≤ 2 at. % Fe. A similar event is seen at higher Fe loads when the N_2 reduction is performed at higher temperatures. During this event, the cellulose matrix is degraded, an ensemble of Ni-Fe magnetic nanoparticles is formed with different distributions of blocking temperatures, and the materials appear to store hydride. For samples for which no energetic event occurs, limited nanoparticle growth and weak magnetic properties are observed. The introduction of Fe into the Ni matrix appears to cause increased magnetic disorder. Both systems have been developed and characterized with the goal of creating magnetically active nanoparticle biocomposites for potential applications in electromagnetic shielding.

2. Keywords

Magnetic nanoparticles, AC magnetic susceptibility, biocomposites, electromagnetic shielding, iron-nickel, iron-palladium

3. Acknowledgements

First and foremost, I would like to thank my faculty co-advisors, Professor Cimpoiasu and CDR Durkin. Their support and commitment to the project and my learning has made the Trident research experience one of the most influential parts of my life. I still recall the day that Professor Cimpoiasu told our Electricity and Magnetism class that she was looking for a student to work in her lab in the next semester. I will always be grateful that I took her up on that offer. I appreciate all of her patience, wisdom, and time that she has generously given me over the last three years. She has thoughtfully guided and mentored me from the first day I showed up in her lab looking cluelessly at data to where I am today. I have enjoyed every part of the research process and being her student. Over the last eighteen months, CDR Durkin has taken it upon himself to convert me from a physicist to a chemist. He has constantly gone out of his way to give me experience in the lab that few (if any) physics students ever receive. I am extremely grateful for his enthusiastic mentorship and the opportunity to blow things up in the lab. I will always appreciate the priority that he has always put on my project and making my Trident experience a positive one.

I would also like to thank all of the contributors from CDR Durkin's research group. Ashlee, of course, thank you for all the time you spent synthesizing, preparing, and characterizing the Fe-Pd samples. After loading a few VSM capsules myself, I know that it wasn't always a quick task. I would like to thank Professor Trulove for his guidance and advice. Thank you to Anders and Mimi for helping us collect last-minute data for the project. Finally, thank you to Chris and Nate for helping me learn the ropes of the lab.

Professor Cimpoiasu acknowledges support from the Office of Naval Research and the Kinnear Fellowship. We thank Prof. Joel Helton for assistance with the ACMS and VSM options of the PPMS. CDR Durkin acknowledges funding from the Air Force Office of Scientific Research. Opinions and conclusions expressed in the study are those of the authors and do not reflect the views of the U.S. Navy or the U.S. Air Force.

4. Table of contents

5. Introduction

At the quantum level, the properties of materials often deviate from their bulk properties as classical physics approximations break down and no longer describe systems well. Nanoparticles are at the forefront of research in science and engineering because of their unique quantum properties and because of their large surface area to volume ratios. When embedded in other materials, nanoparticles can alter and enhance the properties of the resulting composite material. Moreover, the properties of the resulting composites can be tuned by varying the size, composition, distribution, and load of the nanoparticles. These features open the gates to broad applications.

Magnetic nanoparticles, in particular, are of great interest because of the potential to exploit their magnetic properties for applications such as magnetic resonance imaging, drug delivery, data storage, and spintronics [1,2]. Despite many years of research, investigation of the magnetic behavior of magnetic nanoparticles is still ongoing because their properties are not only dependent on their size and atomic composition, but also on the fabrication process and on the matrix in which they are embedded. The fabrication method and the support matrix affect the size, composition, distribution, and load of the nanoparticles which influence the properties of the bulk material [3,4]. Hence, nanoparticle-based composites produced by different fabrication methods and different materials as support matrices should be studied in order to understand which method and support matrix combination results in optimized properties for applications, and to which extent these properties can be further tuned.

There are many choices of solid supporting matrix for the nanoparticles. One category of support that is abundant and structurally favorable is biopolymers (i.e., cotton, linen, silk, etc.). Cellulose, the most common biopolymer, is earth abundant, environmentally sustainable, lightweight, and biodegradable; furthermore, nanoparticles can be nucleated and grown into this biopolymer matrix with a relatively even spatial distribution [5–7]. Cellulose-based composites have a variety of promising applications such as water filtration, fire retardant materials, and electromagnetic shields [6,8,9].

This report details a systematic study of the effects of mass loading on the magnetic properties of Fe-Pd nanoparticles embedded within a cellulose matrix. The Fe-Pd bimetallic system is of particular interest because Fe is ferromagnetic and known for its large magnetization and small coercivity which is useful for applications such as electromagnetic shielding. The presence of Pd serves to prevent oxidation of Fe and encourage the growth of nano-zero valent Fe nanoparticles. The Fe-Pd nanoparticle biocomposites have been previously grown and a spin blocking behavior has been demonstrated [7]. An in-depth characterization of AC and DC magnetic properties is presented in order to identify the physical mechanisms responsible for the magnetism in these materials.

In addition to the Fe-Pd nanoparticle biocomposites, the fabrication and magnetic properties of another magnetic nanoparticle biocomposite, based on Fe-Ni nanoparticles, is reported. Ni, like Fe, is ferromagnetic, and Fe-Ni nanoparticles have been identified as having strong potential for application as electromagnetic shielding materials [10]. Cellulose-based composites containing Fe-Ni nanoparticles have not been studied before, so the Fe-Ni nanoparticle biocoomposite studied in this report is a novel system. Understanding the fundamental building blocks and physicochemical properties of these materials will facilitate the design of novel applications, like electromagnetic shields for DoD applications. Other possible applications include biomedical applications, thermoelectric applications, and joule heating to improve efficiency of nanoparticle catalysis.

6. Experimental section

6.1. Sample preparation

Cotton yarn was milled to powder using a FlackTek Speed Mixer (DAC 150). The appropriate metals (Pd, Fe, Ni, Fe-Pd, and Fe-Ni) were loaded onto cotton powder by incipient wetness (IW) via methods reported in previous studies [5–7], for which metal mass loadings were controlled by altering the metal nitrate concentration in solution. Following IW, the samples were dried on a hot plate at 40 °C, and then sequentially heated under N_2 and H_2 (120 °C for 2 hours in each gas) to reduce the salts and produce alloyed nanoparticles in the biopolymer matrix. Before removal from the tube furnace, the H_2 gas was purged by N_2 gas. Samples were stored in a N_2-filled glovebox until they were ready for further study, and regenerated as needed in the tube furnace. Regeneration was performed using the same process of sequential heating under N_2 and H_2 but the temperature was lowered from 120 °C to 105 °C. Several Fe-Ni samples were reduced at a higher temperature of 200 °C. **Unless otherwise noted, the reduction was performed at 120 °C.**

The label code $\mathrm{Fe_{at.\%}Pd_{at.\%}(wt.\%)}$ is used to distinguish samples. The subscript following the element represents the relative atomic percentage of that metal with respect to the total metal. The parenthetically separated number indicates the wt. % of the metal with respect to the total metal. Theoretical loadings are used for the label codes. For example, in a $Fe_{50}Pd_{50}$(10%) sample, there is are an equal number of Fe and Pd atoms. The (10%) indicates that the combined mass of Fe and Pd represent 10 % of the total mass of the sample. The Fe-Pd samples that are the focus of this study were fixed at the $Fe_{50}Pd_{50}$ composition and the metal load of the sample was varied from 5 % to 30 %. The Fe-Ni samples in this study have been fixed at 20 wt. % while the relative composition of Fe and Ni was altered.

6.2. Material characterization methods

6.2.1. Attenuated total reflection Fourier transform spectroscopy (ATR-FTIR)

Infrared spectroscopy (Thermo Scientific Nicolet iS10) evaluated the chemical composition of the nanoparticle supports. Data (32 scans) were collected from 525 to 4000 $\mathrm{cm^{-1}}$ with 0.421 $\mathrm{cm^{-1}}$ data spacing.

6.2.2. Flame atomic absorption spectroscopy (Flame AAS)

Flame AAS (Perkin Elmer AA Analyst 200) was used to quantitatively measure mass loadings of Pd, Fe, and Ni in each sample. For the Fe-Pd series, powders were extracted from the capsules measured in the physical property measurement system (PPMS). For the Fe-Ni series, ca. 25 mg samples of the bulk powders were used. In both cases, the powders were dissolved in trace metal grade nitric acid, and diluted to the appropriate range of measurement for analysis using class 'A' volumetric glassware and 18.2 MΩ/cm water. Due to the presence of amorphous carbon following sample digestion of Fe-Ni samples, these solutions were filtered with 0.45 µm polyvinylidene fluoride (Millipore) filters prior to analysis.

6.2.3. Scanning electron microscopy (SEM) and energy dispersive x-ray spectroscopy (EDS)

Scanning electron microscopy evaluated sample surface morphology (TESCAN MIRA3 with a TEAM Octane SSD EDS Detector) and EDS provided semi-quantitative measurements of elemental composition. All SEM/EDS data were collected at 20 kV on powdered samples adhered to aluminum stubs with conductive carbon tape.

6.2.4. X-ray diffraction (XRD)

XRD (PANanalytical X'Pert Pro) probed the crystal structure of the nanoparticle biocomposites. Data (30 scans) were collected at 35 kV/30 mA from $2\theta = 5°$ to $90°$ with a step size of 0.01°. GSAS-II software was used to perform a Rietveld refinement and extract the phase ratio.

6.3. Magnetic characterization methods

6.3.1. Vibrating sample magnetometry (VSM)

VSM (Quantum Design physical property measurement system (PPMS) with VSM attachment) was used to characterize the DC magnetic response of the nanoparticle biocomposite. Measurements were performed from 2 - 300 K and the sample vibrated at a frequency of 38 Hz. Magnetization versus temperature measurements were taken in a 250 Oe static field under zero-field-cooled (ZFC) and field-cooled (FC) conditions. Magnetization versus field (up to ±40 kOe) as well as relaxation measurements were taken at various temperatures.

6.3.2. AC magnetic susceptibility measurements

AC magnetic susceptibility measurements (Quantum Design PPMS with AC measurement system II attachment) probed the fine details of the size distribution and magnetic response of the nanoparticles. The in-phase and out-of-phase components of magnetic susceptibility were simultaneously measured from 2 to 300 K in an oscillating magnetic field (with an amplitude of 3 Oe) along with a parallel static field (with a magnitude of 0, 10, 50, 100, or 200 Oe). Measurements were typically taken at eight different frequencies (30, 69, 158, 362, 829, 1902, 4361, and 10000 Hz).

7. Results and discussion for $Fe_{50}Pd_{50}$ nanoparticle biocomposites

7.1. Elemental analysis of $Fe_{50}Pd_{50}$ nanoparticle biocomposites

EDS and Flame AAS were both used to measure the metal load and atomic composition of the Fe-Pd samples (see Table 1). In every case, the measured EDS values for metal load are greater than the values from Flame AA. These differences are attributed to error within the EDS measurement of light elements (i.e., carbon, oxygen, nitrogen) which impact the determination of total metal content in the material. Because Flame-AA could quantitatively determine metal composition of the bulk, that data was used to normalize all of the magnetization measurements that were performed in the PPMS.

Table 1: The data in this table represent the results of Flame AAS and EDS analysis of various Fe-Pd samples.

	Atomic Absorption Spectroscopy Measured Values*				**EDS Measured Values***			
Sample	**Fe (Mass %)**	**Pd (Mass %)**	**Total Mass Metal (%)**	**Atomic % (Fe/(Pd+Fe))***	**Fe (Mass %)**	**Pd (Mass %)**	**Total Mass Metal (%)**	**Atomic % (Fe/(Pd+Fe))**
$Fe_{50}Pd_{50}$(5%)	1.7	3.1	4.8	50.8	2.4	4.5	6.9	50.8
$Fe_{50}Pd_{50}$(10%)	3.3	6.3	9.6	50.2	4.6	8.1	12.7	51.9
$Fe_{50}Pd_{50}$(15%)	4.3	8.9	13.1	47.8	7.8	10.9	18.6	57.7
$Fe_{50}Pd_{50}$(20%)	7.7	15.3	23.0	48.8	11.9	14.9	26.9	60.4
$Fe_{50}Pd_{50}$(30%)	11.5	21.9	33.5	50.0	20.3	23.7	44.0	62.0
Fe_{100}(30%)	27.3	0.0	27.3	100.0	30.0	0.0	30.0	100.0

*Note: Flame AA measurements reflect analysis of samples in triplicate, with RSD of 0.5% in absorbance values. Sample labels reflect theoretical loading of Fe and Pd with respect to each other in atomic percentage and total metal loading in mass percentage with respect to the total matrix (i.e., $Fe_{50}Pd_{50}$(5%) was targeted as 50 at% Fe and 50 at% Pd in cotton fiber at total metal loading of 5 mass%). The samples measured by Flame AA were the exact same samples tested in VSM. The sampes evaluated with EDS were representive powders from the bulk (i.e., not the exact same samples measured in the VSM).

7.2. *Zero-field-cooled (ZFC) and field-cooled (FC) magnetization analysis of $Fe_{50}Pd_{50}$ nanoparticle biocomposites*

7.2.1. *Theory of ZFC and FC magnetization measurements*

Magnetization versus temperature curves generated under ZFC and FC conditions are a common characterization tool that brings insight into the magnetic phenomena in samples with magnetic nanoparticles. In order to understand the results, a brief description of the magnetic model that applies to our ensemble of nanoparticles is helpful. As seen in Fig. 1, bulk materials can be broadly divided into diamagnets, paramagnets, and ferromagnets based on the behavior of their magnetic moments in the presence of a magnetic field H (more exotic magnetic states, like antiferromagnetism or ferrimagnetism will not be discussed here). The average magnetic moment density is called the **magnetization**. Diamagnets are identified by the tendency of the atomic magnetic moments to align in the opposite direction of H while the atomic magnetic moments of paramagnetic materials tend to align along the direction of H. In the absence of a magnetic field, the moments of diamagnetic and paramagnetic atoms tend to align in random directions, resulting in a net magnetization of zero. On the other hand, the spins of neighboring atoms in a ferromagnetic material interact with each other through short-range exchange interactions, causing their magnetic moments to align. A bulk ferromagnetic material is divided into magnetic domains for which the magnetization is oriented along the easy axis of magnetization. Above a certain high temperature, called the Curie temperature, ferromagnetic materials lose their ferromagnetic properties and act like paramagnetic materials as thermal energy overcomes the magnetic ordering.

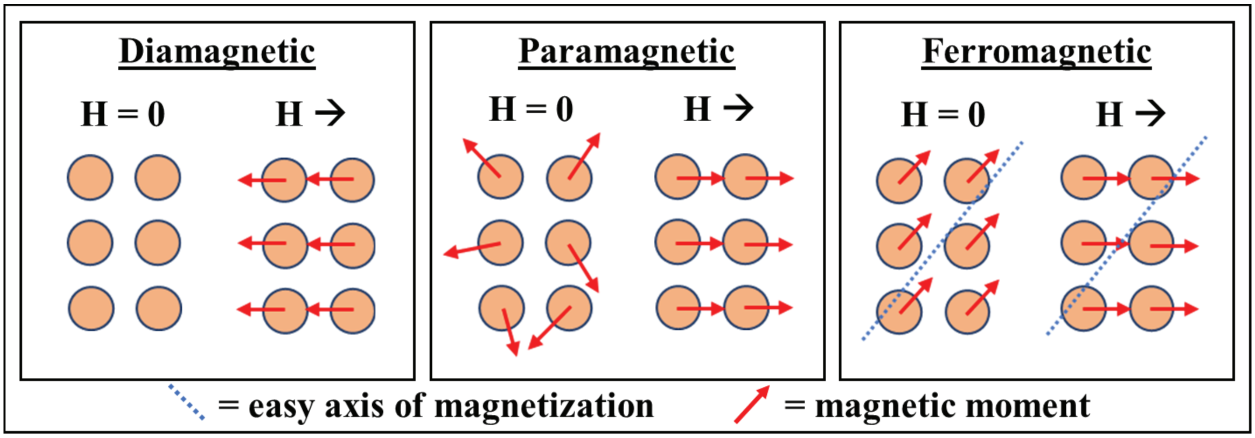

Figure 1: Depiction of magnetic moments of diamagnetic, paramagnetic, and ferromagnetic atoms.

Superparamagnetism is a type of magnetic ordering that occurs far below the Curie temperature in **ensembles of ferromagnetic particles** when the atomic magnetic moments of the particle ferromagnetically align and act as though they have a single collective magnetic moment, like a macrospin. The magnetic moments of macrospins are orders of magnitude greater than atomic magnetic moments. Because iron and nickel are both ferromagnetic materials with Curie temperatures much larger than 300 K and the nanoparticles synthesized in this study are small enough, each nanoparticle is likely composed of one magnetic domain characterized by a giant magnetic moment (or macrospin).

In the absence of external excitations like high temperature or a magnetic field, the macrospin is typically aligned along a preferential direction (the easy axis of magnetization for the particle). When a sample is at room temperature, the macrospins move fast and in all directions because of thermal agitation, such that the average magnetic moment of the sample is very low or zero. When the sample is cooled under zero-field conditions (ZFC), the thermal agitation of the macrospins declines and the spins start to align with the easy axis. At temperatures around 2 K, the spins are frozen in place, either parallel or antiparallel with the easy axis. Since the easy axes are assumed to be relatively randomly oriented, the total magnetization is again zero or very small. As the system of spins is warmed up from 2 K to 300 K under a small applied magnetic field (250 Oe in this study), they acquire enough thermal energy to be free to rotate and align in the direction of the applied magnetic field. Thus, the magnetization increases with increasing temperature. The increase in magnetization continues up to a certain temperature, called the **blocking temperature**, T_B, when the thermal agitation is large enough that the spins escape the interaction with the magnetic field and start again to point in arbitrary directions. Hence, the total magnetization starts to decrease with increasing temperature, much like in the case of a paramagnet. We typically say that the system of spins is “blocked” for temperatures below the blocking temperature. The presence of such a maximum in the ZFC curves is a strong indication of the presence of macrospins and **superparamagnetism** in these samples. When the sample is cooled under field-cooled conditions from room temperature, the macrospins align with the magnetic field more and more as the thermal agitation declines. Therefore, the total magnetization continually increases with decreasing temperature. When all the spins are aligned with the magnetic field, the magnetization saturates and remains constant, despite further decreases in temperature.

Theoretically, T_B can be estimated by considering that the relaxation time, τ, of the spins depends on temperature and the energy barriers to the spin flipping according to Néel’s formula show below in Eqn. 1. In Eqn. 1, E_b represents the magnetic energy barrier to spin flipping, τ_0 is a characteristic spin flipping time with values between 10^{-12} to 10^{-9} sec, k_B is Boltzmann’s constant, and T is the absolute temperature.

$$\tau = \tau_0 \, exp\left(\frac{E_b}{k_B T}\right) \tag{1}$$

During measurement, T_B occurs when the average amount of time it takes for the magnetic moment to flip is the same as the characteristic measuring time τ_m [11]. The blocking temperature can be approximated using the modified Néel-Brown formula given below where K_{eff} is the effective magnetic anisotropy constant, V is the volume of the particle, and U_{int} is the energy from magnetic dipole interactions between particles [11,12].

$$T_B = \frac{E_b}{k_B ln(\frac{\tau_m}{\tau_0})} = \frac{K_{eff}V + U_{int}}{k_B ln(\frac{\tau_m}{\tau_0})} \cong \frac{K_{eff}V + U_{int}}{20k_B} \tag{2}$$

Assuming $\tau_0 = 10^{-11}$ s (well within the typical range of characteristic flip time) and τ_m = 1 s (a typical time to take a measurement using VSM), the approximation of $ln(\tau_m/\tau_0) = 20$ is valid when considering quasi-static measurement times such as those typical in the VSM. For a sample with a monodisperse distribution of nanoparticle sizes, the ZFC curve is sharply peaked, and T_{max}, the temperature associated with the maximum of the curve, can give a good estimate for the average T_B; however, in the case of polydisperse systems, the maximum is not sharp, but rather broad [13,14]. The width of the peak is larger if the distribution is more disperse. In addition, the temperature at which the FC and ZFC curves come together, called the irreversibility temperature, T_{irr}, coincides with T_B for monodisperse samples [15]. The more heterogeneous the system is, the larger the separation between the two characteristic temperatures will be.

In order to model experimental systems that are polydisperse in nature, a distribution of blocking temperatures within the ensemble of nanoparticles is often assumed. The gamma or gaussian functions are both commonly chosen to model the spread of blocking temperatures; however, the lognormal distribution has been selected in this study due to convenient features including not allowing negative values for the blocking temperature [12,14,16,17]. When neglecting interparticle dipole interactions and assuming low magnetic fields, the ZFC and FC magnetization curves can be modeled by the equations below. In this model, M_s represents the saturation magnetization, T_B the blocking temperature, and $f(T_B)$ the distribution of blocking temperatures [11,12,18].

$$M_{ZFC}(T) = \frac{M_s^2 H}{3K_{eff}}\left[ln\left(\frac{\tau_m}{\tau_0}\right)\int_0^T \frac{T_B}{T} f(T_B)dT_B + \int_T^\infty f(T_B)dT_B\right] \tag{3}$$

$$M_{FC}(T) = \frac{M_s^2 H}{3K_{eff}} ln\left(\frac{\tau_m}{\tau_0}\right)\left[\int_0^T \frac{T_B}{T} f(T_B)dT_B + \int_T^\infty f(T_B)dT_B\right] \tag{4}$$

The first and second terms in the equations above represent the contributions from unblocked superparamagnetic moments and blocked moments, respectively. This model is generalized for any distribution, $f(T_B)$, and is applicable to some AC magnetic measurements as well.

7.2.2. Results of ZFC and FC magnetization measurements for $Fe_{50}Pd_{50}$ nanoparticle biocomposites

In Fig. 2, the ZFC and FC curves of five samples with varying metal loads at constant $Fe_{50}Pd_{50}$ composition are shown. The magnetization values are normalized to the combined total mass of iron and palladium in the sample, determined through Flame AAS. The magnitude of the normalized magnetization increases as the load increases suggesting that as the density of metal increases within the supporting matrix, interparticle interactions increase or the magnetic nature of the particles change. There is also a significant evolution of $T_{max} \approx \langle T_B \rangle$ and T_{irr} with load. T_{max} and T_{irr} differ considerably, and the peaks of the ZFC curves are broad, indicating a polydisperse system of nanoparticles. As the metallic load increases, both temperatures increase.

According to Eqn. 2, this indicates that the **effective energy barrier E_b increases**. As summarized in Eqn. 2, the increase in the magnetic energy barrier as the metal load increases is attributed to one or a combination of the following mechanisms: (1) an increase in interactions U_{int} between macrospins as the density of particles increases, (2) an increase in the size, V, of particles, or (3) an increase in the K_{eff} anisotropic energy density due to changes in shape or composition of particles.

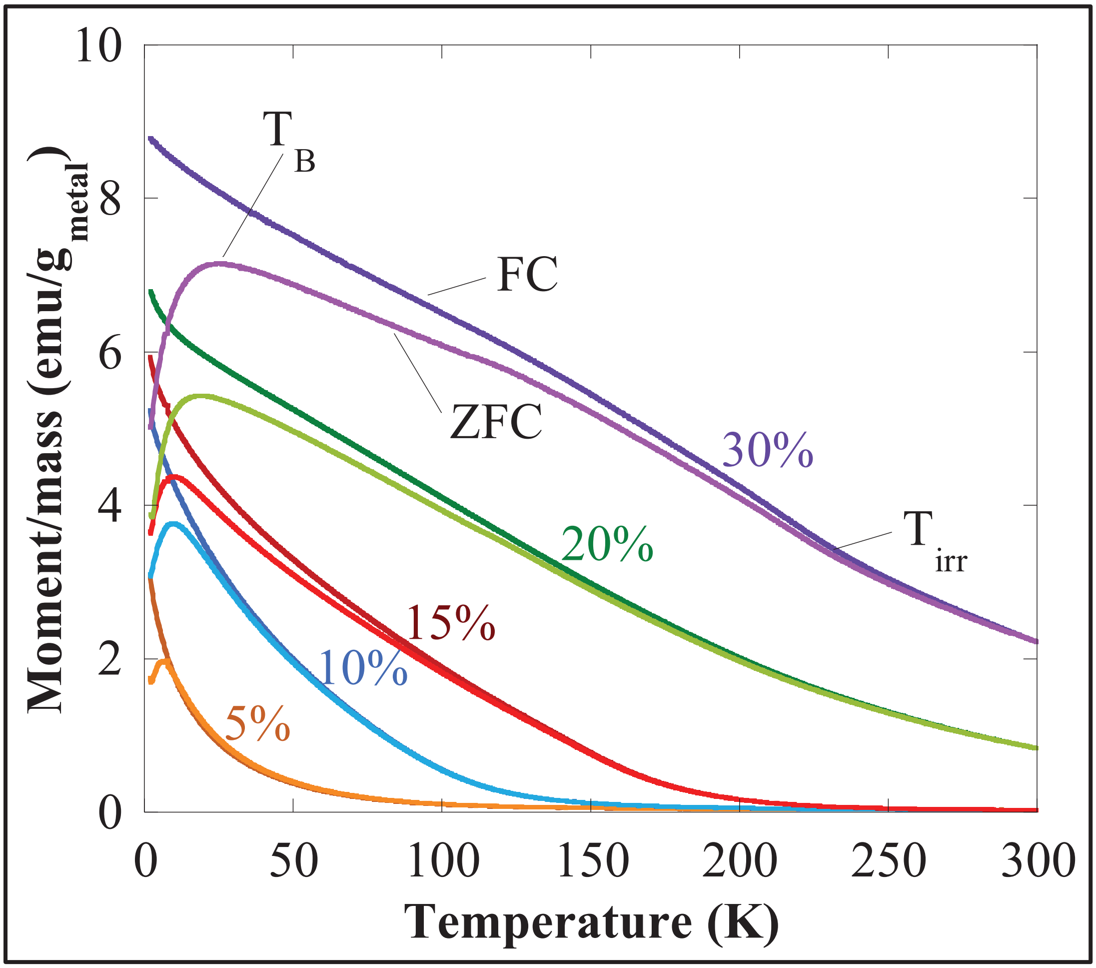

Figure 2: Zero-field-cooled (ZFC) and field-cooled (FC) magnetization curves of the $Fe_{50}Pd_{50}$ series from 2 K to 300 K under a static 250 Oe field. The magnetic moment has been normalized to the combined mass of Fe and Pd in the sample using the compositions calculated from AAS measurements. The blocking temperature T_B and irreversibility temperature T_{irr} have been identified on the $Fe_{50}Pd_{50}$(30%) curve.

7.3. Magnetization versus DC field analysis of $Fe_{50}Pd_{50}$ nanoparticle biocomposites

Magnetization, *M*, hysteresis loops generated by varying the DC field, *H*, are another common tool used to characterize ensembles of magnetic nanoparticles. The shape of this hysteresis is used as a quick indicator of the nature of magnetic interaction in the system. For instance, a fully reversible *M* vs *H* curve suggests a paramagnetic material, when the spins align with the field and the inter-spin interaction is negligible. The hysteresis of a ferromagnetic material is large, mainly due to the strong exchange interaction between the spins. An M vs. H curve that is sigmoidal in shape with minimal irreversibility is a signature of a **superparamagnetic** material. The sigmoidal shape is observed because ensembles of single domain particles interact similarly to a paramagnetic material, except that the magnitude of the particles macrospins are much larger compared to the typical magnetic moments in a paramagnet. As seen in the selected $Fe_{50}Pd_{50}$ M vs. H curves in Fig. 3, the sigmoidal shapes of each hysteresis loop demonstrate that the material exhibits typical superparamagnetic behavior. The temperature-dependent coercive fields and remnant magnetization for selected $Fe_{50}Pd_{50}$ samples are shown in Fig. 4. These values are small, consistent with a system of nanoparticles with generally weak interparticle interactions. At times, a negative remnant magnetization has been observed. This is attributed to a well-documented measurement error within the PPMS when transitioning from high fields (> 1000 Oe) to low fields (< 20 Oe) [19]. The increase of coercivity and remnant magnetization with increasing the metallic load confirms that the interparticle magnetic interaction is enhanced when the metallic density increases, in line with observations of increased T_B.

It is also notable that even at the maximum applied field of 40 kOe, the saturation magnetization has not been reached. This is easiest to observe for T = 2 K. Rather than asymptotically approaching saturation, the magnetization increases with field almost linearly above 20 kOe. The additional linear increase of the magnetization suggests nonuniformity within the material. This could be attributed to a core-shell model of nanoparticles where a magnetically ordered core is surrounded by a disordered shell, though further analysis of nanoparticle structure (i.e., TEM) would be needed to confirm.

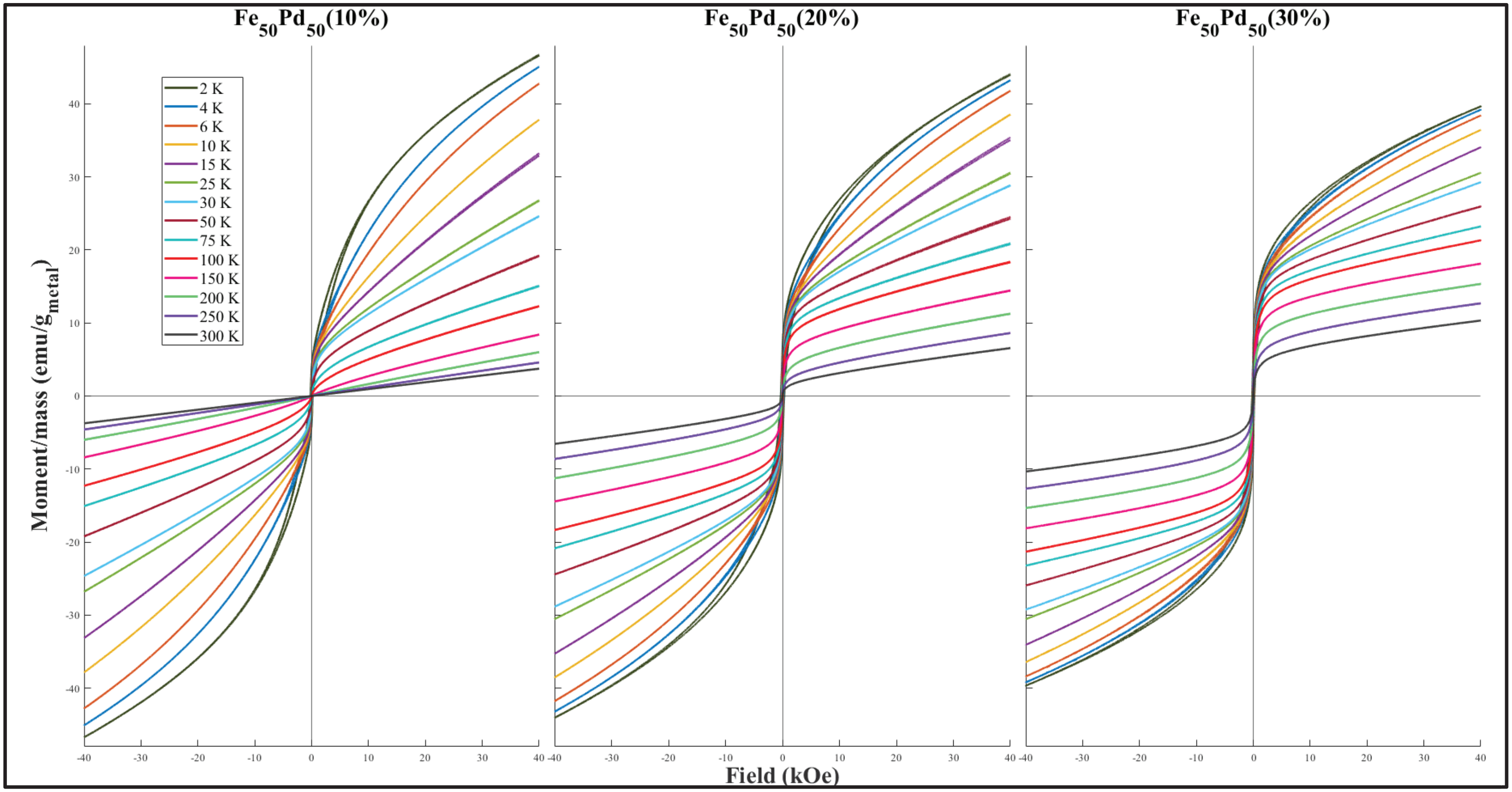

Figure 3: Magnetization versus magnetic field data is shown for selected $Fe_{50}Pd_{50}$ samples. The magnetic moment has been normalized to the combined mass of Fe and Pd in the sample using the compositions calculated from AAS measurements.

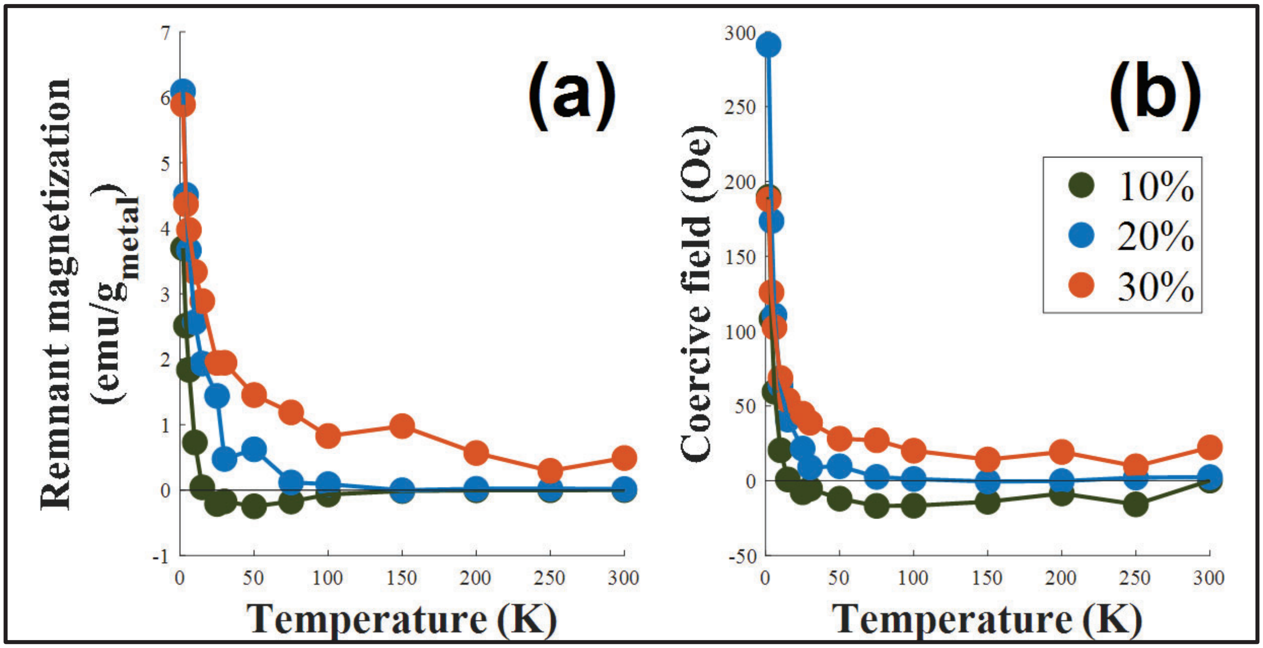

Figure 4: Magnetic remanence versus temperature (a) and coercivity versus temperature (b) for selected $Fe_{50}Pd_{50}$ samples. Both quantities are extracted from M vs. H measurements. The magnetic moment has been normalized to the combined mass of Fe and Pd in the sample using the compositions calculated from AAS measurements.

7.4. AC magnetic susceptibility analysis of $Fe_{50}Pd_{50}$ nanoparticle biocomposites

7.4.1. Theory of AC magnetic susceptibility measurements

As discussed above, the magnetization is the net magnetic moment within a sample normalized to the volume of the sample. When a magnetic field is applied in a given direction, it becomes energetically favorable for the magnetic moments to point in the direction of the applied field. A quantity called the **magnetic susceptibility**, χ, represents the change of the magnetization, M, with respect to the applied magnetic field, H as shown in Eqn. 5.

$$\chi = \frac{dM}{dH} \tag{5}$$

The details of the magnetic response of the nanoparticle biocomposite were determined by measuring the susceptibility while applying a magnetic field with both a static and oscillating component. While measurements in a static field can be a good gauge of the basic magnetic properties of a system, the **magnetic susceptibility is a far more sensitive tool to understand the intricacies of an ensemble of nanoparticles**. For all the susceptibility measurements in this study, the amplitude of the oscillating field was kept constant at 3 Oe and the magnitude of the static field was varied between 0 and 200 Oe. The field can be described with Eqn. 6 where H is the real component of the total magnetic field, H_0 is the magnitude of the static field, h is the amplitude of the oscillating field, $\omega = 2\pi f$ is the angular frequency of the oscillating field, and t is the time [20].

$$H = Re[H_0 + he^{i\omega t}] = H_0 + h\cos(\omega t) \tag{6}$$

In this case, the real component of magnetization, M, is given by Eqn. 7 where M_0 is the magnetization corresponding to the static field, m is the magnetization corresponding to the oscillating field, and θ represents the lag between the magnetization and the oscillating field.

$$M = \mathrm{Re}[\mathrm{M}_0 + \ me^{i(\omega t-\theta)}] = \mathrm{M}_0 + m\cos(\omega t - \theta) \tag{7}$$

From these definitions of magnetization and field, χ can be determined using time derivatives of the complex definitions of magnetization and field shown in Eqns. 6 and 7. This is shown below in Eqn. 8.

$$\chi = \frac{dM}{dH} = \frac{dM/dt}{dH/dt} = \frac{m}{h}(\cos(\theta) - i\sin(\theta)) \tag{8}$$

The susceptibility is typically parameterized as having a real component, χ', that is in phase with the oscillating field as well as an imaginary, out-of-phase component, χ'' as shown in Eqn. 9. These components are given below in Eqn. 10 and 11.

$$\chi = \chi' - i\chi'' \tag{9}$$

$$\chi' = \frac{m}{h}\cos(\theta) \tag{10}$$

$$\chi'' = \frac{m}{h}\sin(\theta) \tag{11}$$

Separating the in-phase component from the out-of-phase component of susceptibility is particularly helpful in interpreting the physical meaning of the magnetic susceptibility. For example, the χ'' component is closely associated with energy dissipation and losses. For applications such as electromagnetic shielding, χ'' demonstrates the capacity for a material to absorb energy from an incoming electromagnetic wave. As seen in the relationship encapsulated in Eqn. 12, the average power absorbed in one period, *T*, is proportional to the magnitude of χ''.

$$P_{avg} = \frac{1}{T}\int_0^T h\frac{dm}{dt}dt = \frac{1}{2}\omega h^2\chi'' \tag{12}$$

In the simplest case, an ensemble of magnetic nanoparticles is assumed to have a monodisperse shape and size, and therefore a single τ and T_B. The relaxation or flip time of the macrospins, τ, is typically defined by Néel's formula in Eqn. 1. In the monodisperse case, χ' and χ'' are given by the equations below, where χ_0 represents the static susceptibility [21].

$$\chi' = \chi_0 \frac{1}{1+(\omega\tau)^2} \tag{13}$$

$$\chi'' = \chi_0 \frac{\omega\tau}{1+(\omega\tau)^2} \tag{14}$$

However, few experimental nanoparticle ensembles are truly monodispersed. Instead, a polydisperse range of particle shapes, anisotropies, and sizes results in a system that is effectively modeled by a distribution of blocking temperatures. χ'' is modeled by integrating Eqn. 14 over all possible blocking temperatures in a lognormal distribution of blocking temperatures, $P(\theta)$, shown in Eqn. 15. The resulting expression of χ'' for N particles is shown in Eqn. 16. To declutter the expression, each possible magnetic energy barrier in the distribution (KV/k_B) is represented by θ. θ_0 is used to describe the median energy barrier of the distribution in units of temperature. The broadness of each blocking temperature distribution is defined by δ_θ, which is approximately the root mean square deviation of the blocking temperature. If a spherical particle is assumed, the spread of the diameters of the particles, δ_D, is proportional $(3\delta_D \approx \delta_\theta)$ to the spread of the blocking temperatures. This approximation is only valid if a lognormal distribution is used.

$$P(\theta) = \frac{1}{\sqrt{2\pi}\theta\delta_\theta} exp\left(-\frac{ln^2(\theta/\theta_0)}{2\delta_\theta^2}\right) \tag{15}$$

$$\chi'' = N\chi_0 \int_0^\infty \frac{\theta^2}{\theta_0^2} \frac{\omega\tau(\theta\ /T)}{1+[\omega\tau(\theta\ /T)]^2} P(\theta) d\theta \tag{16}$$

As laid out in Ref. 14, this model can be extended even further for heterogenous samples with n lognormal distributions of blocking temperatures. The susceptibility found in Eqn. 14 can be approximated to a delta function centered on σ^*, defined in Eqn. 17. This allows the integral in Eqn. 16 to be simplified to the form in Eqn. 20. This approximation holds for samples with a broad distributions of blocking temperatures (δ_θ > 0.25) and low frequencies of oscillation (f < 10000 Hz).

$$\sigma^* = -ln(\omega\tau_0) = -ln(2\pi f\tau_0) \tag{17}$$

If the contributions from the dipolar interaction are neglected, θ^* is given by Eqn. 18. If contributions from the dipolar interaction are accounted for in the parameter γ, θ^* can be defined by Eqn. 19. The parameter γ is a second order term based on the mean field model of the dipolar interaction. It is proportional to the strength of the dipolar interaction, and Eqn. 19 holds for small values of γ ($0 \leq \gamma < 0.2$).

$$\theta^* = \sigma^* T = -T ln(2\pi f\tau_0) \tag{18}$$

$$\theta^* = \frac{T}{2\gamma}\sqrt{1-4\gamma ln(2\pi f\tau_0)} - 1 \tag{19}$$

The frequency dependence of the maximum of the χ'' curves has been consolidated into the function ψ, which also depends on γ when the dipolar interaction is considered. The ψ-dependence of the χ'' curve can be removed by normalizing all the χ'' curves to the maximum value. The constant c is defined in Eqn. 21 and depends on the number of particles, N, saturation magnetization, M_s, median volume of the nanoparticles, V_0, Boltzmann's constant, k_B, and δ_θ. The median energy barrier for the i^{th} distribution of blocking temperatures is $\theta_{0,i}$ as defined in Eqn. 22 in units of temperature. Finally, the fraction of particles in the i^{th} distribution is given by q_i.

$$\chi'' = \frac{M''}{H} = \psi(f,\gamma)\sum_{i=1}^{n} c_i q_i \frac{\theta^*}{\theta_{0,i}} exp\left(-\frac{ln^2(\theta^*/\theta_{0,i})}{2\delta_{\theta,i}^2}\right) \tag{20}$$

$$c_i = \sqrt{\frac{\pi}{8}}\frac{\chi_{0,i}}{\delta_{\theta,i}} = \sqrt{\frac{\pi}{2}} N\left(M_s V_{0,i}\right)^2/(6k_B\delta_{\theta,i}) \tag{21}$$

$$\theta_{0,i} = \frac{E_{B,i}}{k_B} \tag{22}$$

7.4.2. Metallic load dependence of susceptibility at constant static field for $Fe_{50}Pd_{50}$ nanoparticle biocomposites

Measurement of the χ' and χ'' components of magnetization under a 10 Oe static field can be seen in Fig. 5. All samples pictured are the $Fe_{50}Pd_{50}$ composition and the load increases from left to right. The sample is demagnetized and cooled under no field, so the ZFC magnetization model in Eqn. 3 is used to understand the χ' curves. Similar features to the ZFC/FC data presented in Fig. 2 are observed including an increasing magnitude of χ' as well as a shift to the right in the peak of χ' as the load increases. **This corresponds to a stronger magnetic response and increasing average T_B as the frequency increases**. As expected in a typical system of magnetic nanoparticles, the χ' curve monotonically decreases in magnitude as frequency increases. An increasing frequency represents a decrease in τ_m, which physically means that the magnetic field has less time to push magnetic moments in a given direction before the field flips direction itself. This is also predicted by the Eqn. 3 model for ZFC magnetization, where a decrease in τ_m causes a decrease in magnitude of the unblocked moments and a decrease in amplitude of magnetization. Another feature that is predicted by this model is that the frequency dependence is most visible around T_B. At low temperatures, the term that represents the contribution from the blocked moments dominates over the unblocked moments. In the Eqn. 3 model, this term has no frequency dependence. At higher temperatures, particularly those where $T \gg T_B$, the frequency dependent term representing the unblocked moments is driven to zero. This feature is evident in the $Fe_{50}Pd_{50}$(10%) and $Fe_{50}Pd_{50}$(15%) samples as the χ' curves at various frequencies start together, fan out near the peak of χ' , and collapse back together above T_B.

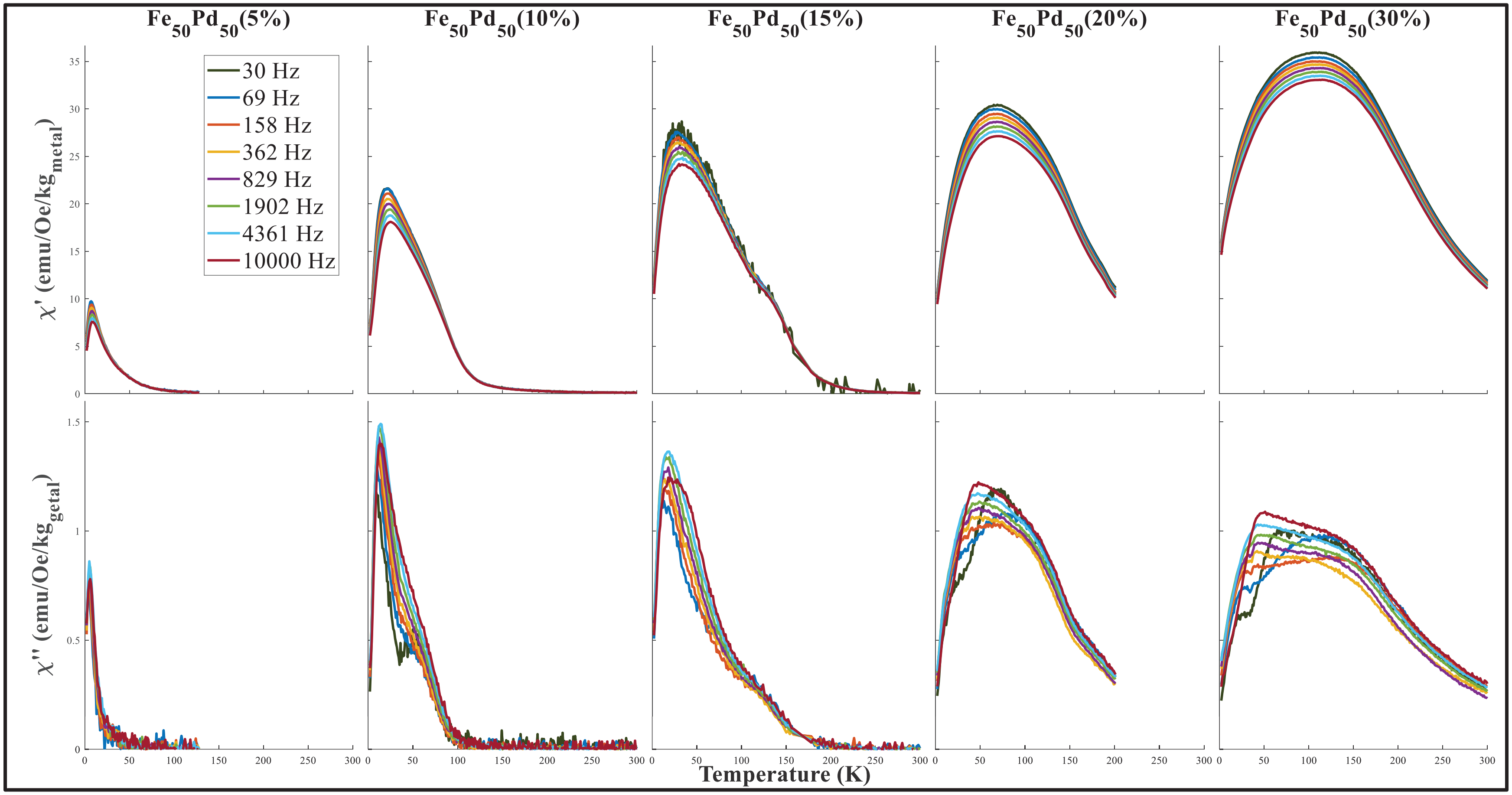

Figure 5: In-phase (χ′) and out-of-phase (χ′′) components of AC magnetic susceptibility versus temperature at constant static field of H_0 = 10 Oe. Metallic load increases from left to right. The amplitude of the oscillating field, h, is 3 Oe. The frequency of oscillating field was varied between the eight different frequencies indicated in the legend. The susceptibility has been normalized to the combined mass of Fe and Pd in the sample using the compositions calculated from AAS measurements.

In a monodisperse system of nanoparticles, a single peak in the χ'' curve is expected at the blocking temperature. In the $Fe_{50}Pd_{50}$ samples, a much more complex picture emerges, particularly at loads above 5 wt. %. Instead of just one peak in χ'', there is evidence of **several frequency dependent peaks, particularly at higher loads**. At the same time, the general shape of the χ'' curve noticeably broadens and shifts to the right as the metallic load increases, a trend that is consistent with data collected at other static fields (not pictured). The broadening and rightward shift indicate increasing heterogeneity and an increase in the average T_B as the metallic load increases. This supports the conclusions from the ZFC and FC data. However, more nuance about the magnetic structure of the nanoparticle biocomposites is revealed through the examination of the χ'' peaks' evolution with field, load, and frequency.

7.4.3. Static field dependence of χ at constant metallic load for $Fe_{50}Pd_{50}$ nanoparticle biocomposites

Fig. 6 shows a set of χ' and χ'' curves measured at different static fields (H_0) from the same $Fe_{50}Pd_{50}$(10%) sample. The first feature that is evident from these data is that the magnitude – but not the sign – of the applied field affects the χ' and χ'' curves. In particular, the curves measured at -10 Oe and + 10 Oe are identical to one another. As the magnitude of the static field increases, χ' and χ'' monotonically decrease. Because the susceptibility can be thought of as the derivative of the M vs. H hysteresis loop, this result is expected. As can be seen in Fig. 3, the slope of the M vs. H curve decreases as field increases. As the magnetic field increases in strength, more spins tend to align with the field rather than with their easy axis. Hence, when a stronger static field is applied, fewer spins are affected by the very small (3 Oe) oscillating field, so both the in-phase and out-of-phase components of χ are expected to drop.

7.4.4. Identifying peaks in χ'' for $Fe_{50}Pd_{50}$ nanoparticle biocomposites

One area of particular interest in this research was identifying and characterizing the evolution of different peaks in the χ'' curves. **Each of these peaks corresponds to a separate distribution of blocking temperatures, which correspond to a distinct group of particles with similar properties.** Therefore, the χ'' data can be used to characterize the nanoparticles within the biocomposite. The evolution of these peaks with frequency, static field, and load is summarized in Fig. 7. The $Fe_{50}Pd_{50}$(10%), $Fe_{50}Pd_{50}$(20%), and $Fe_{50}Pd_{50}$(30%) curves are shown with metallic load increasing from top to bottom while the static field (H_0) increases from left to right. In total, **four** separate peaks have been identified within these samples. Each peak corresponds to a different color as annotated in the legend. Each arrow indicates the approximate T_{max} of each peak at the peak's maximum frequency, f_{max}. Because the peaks are located so close to one another, it is sometimes difficult to evaluate them separately. In particular, the interference complicates the determination of the absolute and relative magnitude of individual peaks.

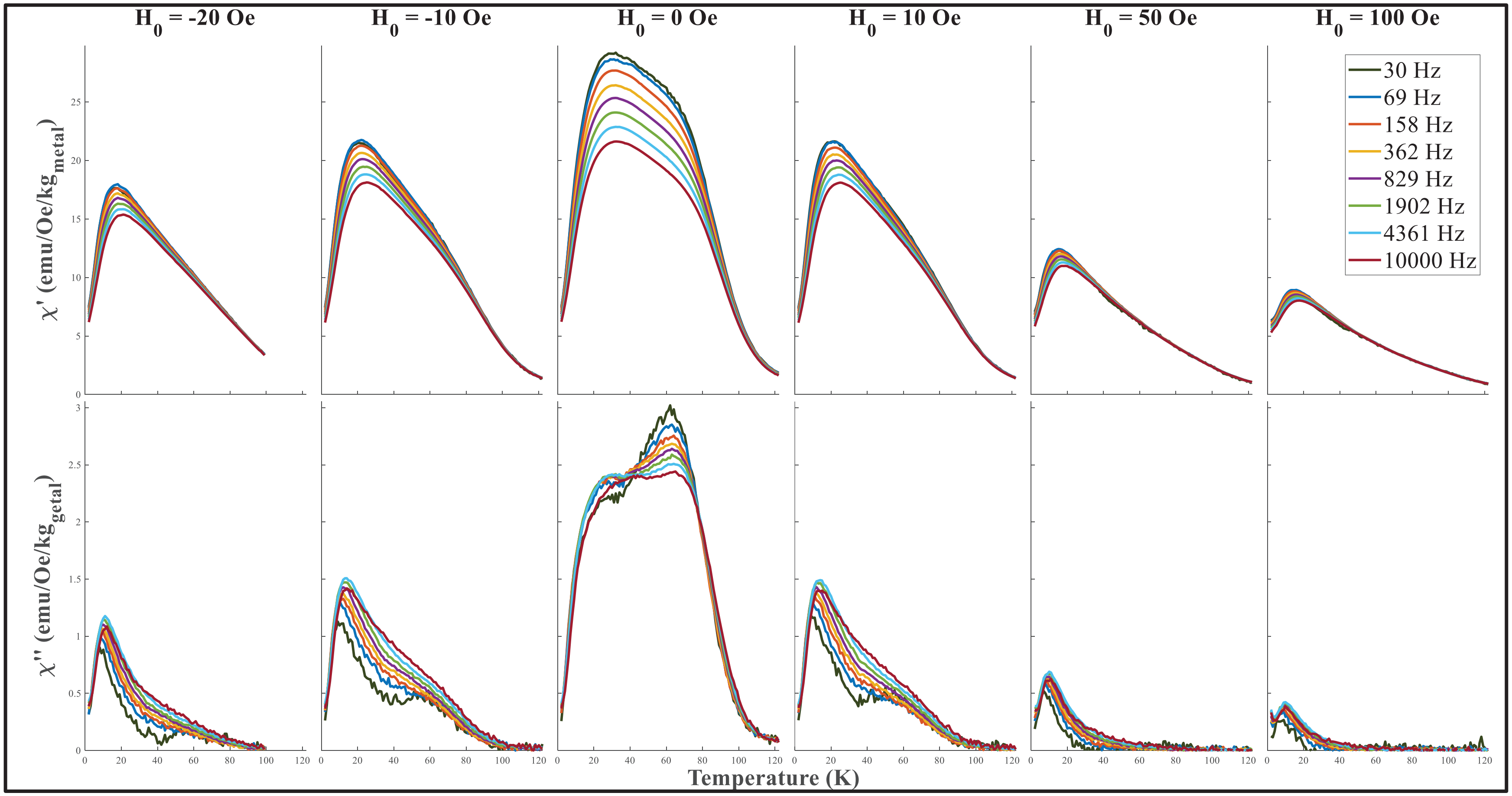

Figure 6: Out-of-phase (χ'') AC susceptibility data for $Fe_{50}Pd_{50}$(10%) at varying static fields. Static field increases from left to right. The amplitude of the oscillating field, h, is 3 Oe. The frequency of the oscillating magnetic field was varied between the eight different frequencies indicated in the legend. The susceptibility has been normalized to the combined mass of Fe and Pd in the sample using the compositions calculated from AAS measurements.

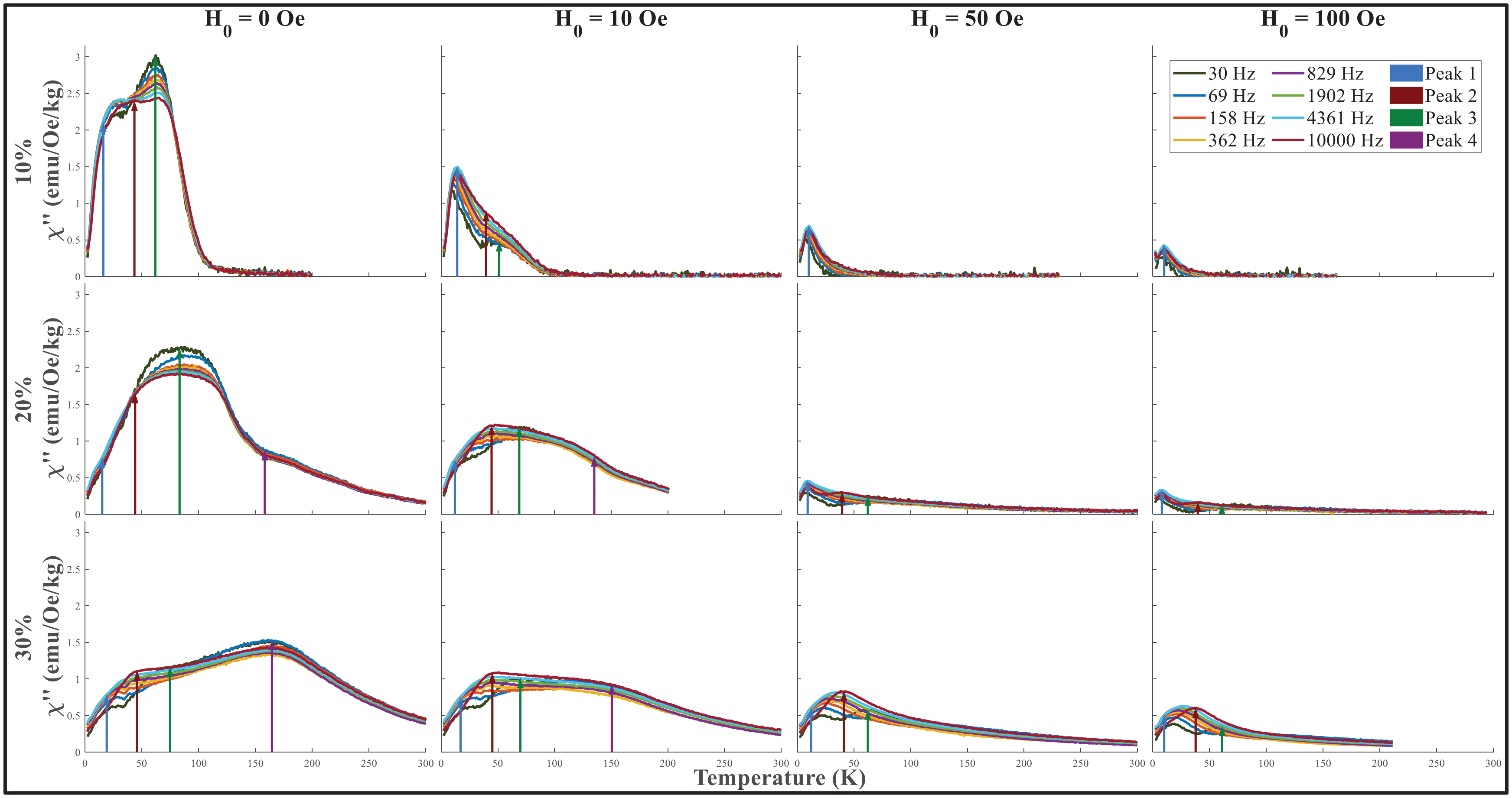

Figure 7: Out-of-phase (χ'') AC magnetic susceptibility data for the $Fe_{50}Pd_{50}$(10%), $Fe_{50}Pd_{50}$(20%), and $Fe_{50}Pd_{50}$(30%) samples at varying static fields. Static field increases from left to right. Arrows indicate the hypothesized maximum position of four different peaks in χ''. The amplitude of the oscillating field, h, is 3 Oe. The frequency of oscillating field was varied between the eight different frequencies indicated in the legend. The susceptibility has been normalized to the combined mass of Fe and Pd in the sample using the compositions calculated from AAS measurements.

7.4.5. Frequency dependence of peaks in χ'' for $Fe_{50}Pd_{50}$ nanoparticle biocomposites

Intriguingly, each peak evolves slightly differently with frequency. The frequency dependence of each peak in summarized in Fig. 8. The frequency dependence of each peak is nearly identical at different loads and static fields, a property that has allowed us to distinguish and identify peaks.

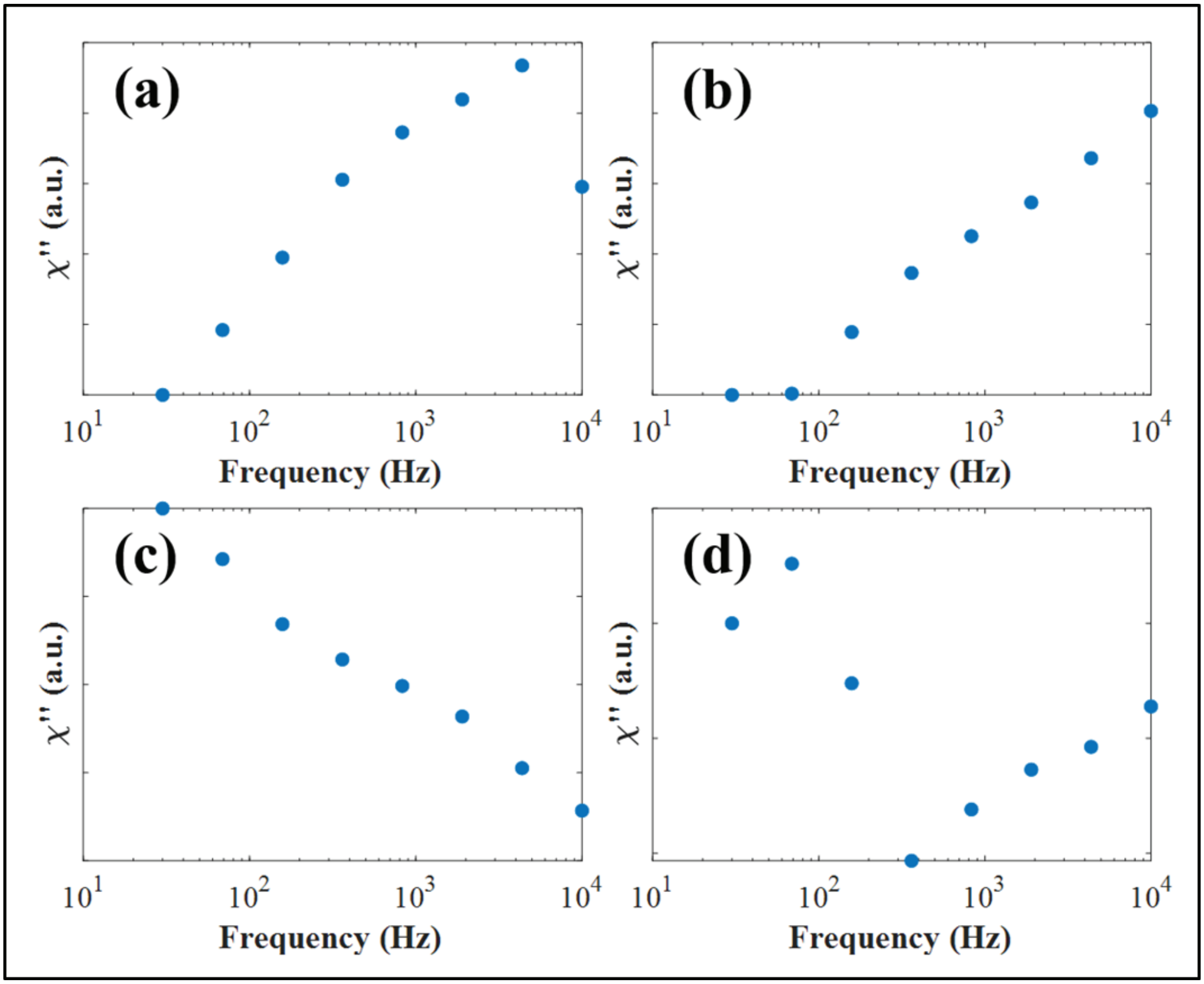

Figure 8: The frequency dependence of each peak (peaks 1-4 listed in a-d, respectively) is indicated in the figure above. Each panel represents data taken from a single sample at a constant temperature and field. The sample and field for which that respective peak is most visible and has the least interference from neighboring peaks has been chosen. In (a), data at 10 K from $Fe_{50}Pd_{50}$(10%) at 50 Oe was selected to represent peak 1. In (b), data at 45 K from $Fe_{50}Pd_{50}$(30%) at 10 Oe was selected to represent peak 2. In (c), data at 63 K from $Fe_{50}Pd_{50}$(10%) at 0 Oe was selected to represent peak 3. In (d), data at 166 K from $Fe_{50}Pd_{50}$(30%) at 0 Oe was selected to represent peak 4.

The frequency at which the χ'' peak is at its maximum can be taken as a good approximation of the reciprocal of the relaxation time. Therefore, Eqn. 1 can be rewritten as the following where $\omega_{\max} = 2\pi f_{max}$ represents the maximum frequency.

$$-k_B T ln(\omega_{\max}\tau_0) \cong K_{eff}V = E_b \qquad (23)$$

Therefore, by estimating the value of τ_0 and using the T_{max} and f_{max} determined from the data in Fig. 7, the value of the energy barrier can be estimated of each group of particles. In order to perform a rough quantification of the physical meanings of this energy barrier, values of K_{eff} have been estimated by assuming a constant V across the four peaks. The V chosen was selected based on prior TEM analysis of the Fe-Pd system [7]. Next, instead of assuming a constant V, the K_{eff} was assumed to be constant, and an estimation of the values of V was completed. The value of K_{eff} for this estimation was selected based on analysis of similar systems in the literature [4]. Results from these estimates can be seen in Table 2. In reality, both K_{eff} and V may vary from peak to peak, but the estimates in Table 2 give an approximation of the distribution of nanoparticles. When K_{eff} was assumed to be constant, the nanoparticle size is clustered around 5 nm, in agreement with TEM observations. If the assumption of ca. 5 nm nanoparticle size is taken from the TEM data, the range of K_{eff} values are on the order of similar iron nanoparticles in the literature [4].

Within each peak, the T_{max} shifts to the right as frequency increases. This indicates that the blocking temperature increases as the τ_m decreases. This is encapsulated in the definition of blocking temperature in Eqn. 3. The trend is also consistent with the well-established relationship between blocking temperature and frequency [14,22].

Table 2: Data in the first two rows of this table represent the values calculated directly from the data encapsulated in Fig. 7. The following rows are calculated using Eqn. 22 and the assumptions shown above.

	Peak 1	**Peak 2**	**Peak 3**	**Peak 4**
T_{max} (K)	8-15	35-45	60-85	150-165
f_{max} (Hz)	3000 ± 1000	> 10000	< 30	50 ± 30
E_B (eV) *	0.013	< 0.041	> 0.12	0.23
V (nm^3) **	21	< 66	> 190	370
d (nm) **	3.4	< 5.0	> 7.1	8.9
K (kerg/cm^3) ***	320	< 1000	> 3000	5700

* Assume $\tau_0 = 10^{-10}$ s

** Assume $\tau_0 = 10^{-10}$ s; K = 1000 kerg/cm^3

*** Assume $\tau_0 = 10^{-10}$ s V = 65 nm^3 (d = 5 nm)

7.4.6. Total metallic load dependence of peaks in χ'' for $Fe_{50}Pd_{50}$ nanoparticle biocomposites

With few exceptions, the T_{max} of each peak, and therefore the median blocking temperature of the given distribution of particles, increases with increasing Fe-Pd metal load. When the metallic load increases, it can be assumed that the interparticle spacing decreases and the particle density increases. **Therefore, stronger dipolar interactions between particles are expected as the metal load increases.** Although some models predict that a stronger dipolar interaction will lead to a decrease in the blocking temperature, the vast majority of experimental evidence supports models that predict an increase in T_B as the dipolar interaction increases [4,14,18,23]. **The increase in T_B may also be attributed to agglomeration of smaller particles into larger, more magnetically ordered particles or clusters of particles.** Increasing agglomeration as load increases has been observed in past studies of Fe-Pd nanoparticle biocomposites and similar biocomposites [5,7]. From Eqn. 2, larger particles are clearly linked to an increase in E_B, T_B, and therefore T_{max}.

7.4.7. Static field dependence of peaks in χ'' for $Fe_{50}Pd_{50}$ nanoparticle biocomposites

The T_{max} of each peak tends to decrease with increasing applied field. The static field dependence of the blocking temperature is commonly modeled as shown below in Eqn. 24 where h^* is defined in Eqn. 25 and proportional to the static field. A decrease in T_B, T_{max}, and the energy barrier is predicted as the static magnetic field increases [13,22,24,25].

$$T_B = \frac{KV(1-h^*)^2}{k_B \ln(\tau_m/\tau_0)} \tag{24}$$

$$h^* = \frac{2H_0K}{\mu_0 M_s} \tag{25}$$

7.4.8. Estimation of τ_0 for 1st peak using Arrhenius plot for $Fe_{50}Pd_{50}$ nanoparticle biocomposites

One of the characteristic parameters used to describe a magnetic nanoparticle is its **characteristic flip time**, τ_0. After determining a particle's T_B and τ_0, Eqn. 1 can be used to predict how often the spin of the particle will flip orientation at any given temperature. The standard method for determining τ_0, stipulates creating an Arrhenius plot relating T_{max} to the frequency of the oscillating field, f. However, this method is primarily limited to monodisperse and non-interacting systems that have a single, clear peak in χ''. For most of the panels in Fig. 7, this is clearly not the case as multiple overlapping peaks are present. **As expected, the Arrhenius plots for most peaks generally have poor linearity and non-physical values for τ_0**, indicating that this method is not readily applicable to multiple peaks that are interfering with one another. However, the 50 Oe and 100 Oe curves for the $Fe_{50}Pd_{50}$(10%) sample are both dominated by the first peak and appear to have negligible contributions from other peaks. Therefore, these two datasets have been chosen to perform Arrhenius plot estimations of τ_0. The Arrhenius plots, shown in Fig. 9, are linear ($R^2 = 0.9872$ and 0.9781, respectively) and indicate that the value of τ_0 for the particles corresponding to the first peak are ≈ 2 x 10^{-11} s. While a small evolution of τ_0 is expected at different static fields even for the sample peak and the same sample [26], the analysis in this report indicates the τ_0 for a given peak and sample remains relatively constant as the static field is varied.

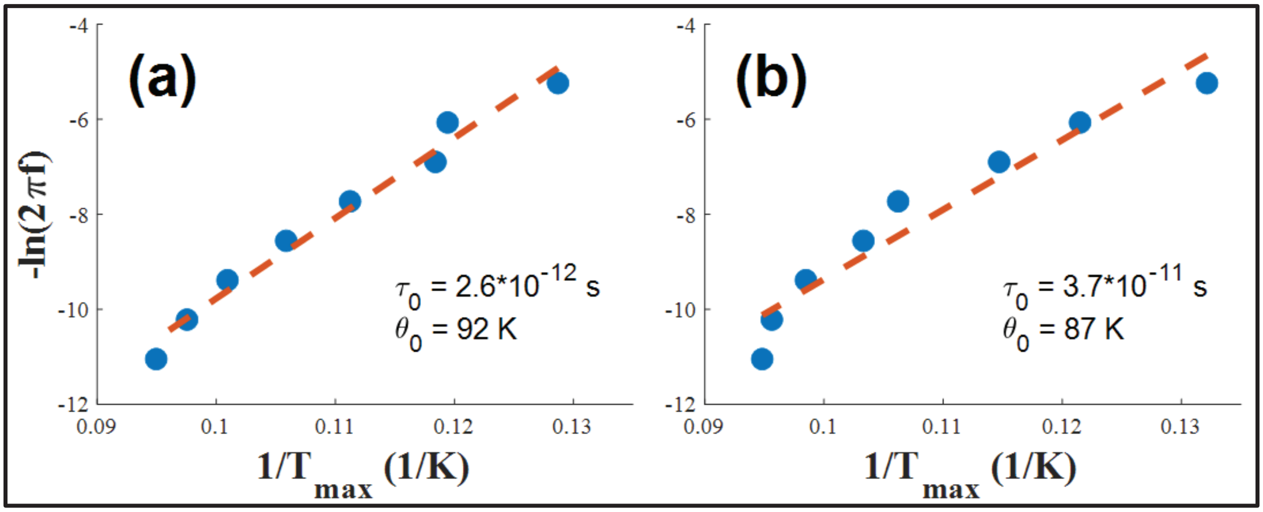

Figure 9: Arrhenius plots for the first peak of χ'' of $Fe_{50}Pd_{50}$(10%) at (a) H_0= 50 Oe and (b) H_0= 100 Oe. The values for τ_0 and θ_0 calculated from the Arrhenius plot are listed on each panel. The δ_D calculated from the fit in Fig. 12 was used to determine the values for θ_0.

7.4.9. Estimation of τ_0 and dipolar interaction for 1st peak using data collapse for $Fe_{50}Pd_{50}$ nanoparticle biocomposites

Recently, different methods for extracting τ_0 [16] and quantifying the dipolar interactions have been developed [14] that involve performing a data collapse of normalized χ'' curves at different frequencies when plotted as a function of θ^* as defined in Eqn. 18 and 19. The advantage of the data collapse method is while Arrhenius plots use just a single data point from each frequency curve (the maximum), the data collapse method uses the **entire curve** to estimate τ_0. Therefore, the collapse method has the potential to be more accurate in determining τ_0. The data collapse method was employed to investigate the $Fe_{50}Pd_{50}$(10%) sample at H_0 = 50 Oe and H_0 = 100 Oe using the Eqn. 19 model for θ^*. It was found that γ was equal to zero, implying that **the strength of the dipolar interaction was not significant at the 50 Oe or 100 Oe trials of the $Fe_{50}Pd_{50}$(10%) sample**. The resulting data collapse and extracted values can be seen in Fig. 10. The resulting τ_0 calculated (≈ 6 x 10^{-11} s) was similar to the 2 x 10^{-11} s calculated using the Arrhenius plot method.

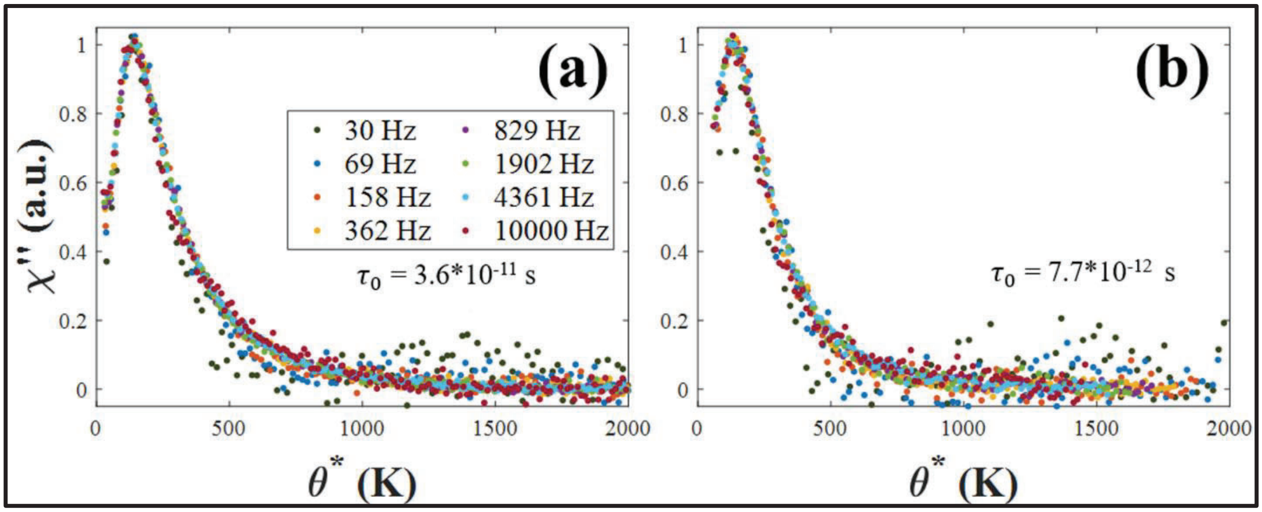

Figure 10: The figure shows the results of a data collapse of χ'' performed on the $Fe_{50}Pd_{50}$(10%) sample at (a) H_0= 50 Oe and (b) H_0= 100 Oe. Each of the curves generated from eight frequencies seen in the legend below was normalized to its maximum value and then collapsed onto a single curve using the Eqn. 19 model for θ^*. For both cases, $\gamma = 0$ and the value of τ_0 is annotated on the plot. Data from T = 2 K to 150 K was used in the collapse.

After completing analysis of the simplest cases of the 10 % sample at 50 Oe and 100 Oe, the first peak at 10 Oe at a range of loads was evaluated. A data collapse was performed on a range of data from 2 K to a temperature between the T_{max} of the first and second peak (around 25 K). In this way, the first peak could be studied while eliminating interference from the second peak. First, the Eqn. 18 model neglecting the dipolar interaction was used. The results are summarized in Table 3. The general trend observed was a **decreasing τ_0 as the metal load increased.** At higher loads, the values began to decrease to nearly unphysical values below 10^{-12} s, as is common when neglecting dipolar interactions [4,14].

Table 3: Data in this table reflect τ_0 values for the first peak of selected samples at 10 Oe. The values were calculated using the collapse method of just the first peak. Raw data from 2 K to 25 K was used in order to isolate contributions from only the first peak.

Sample	**τ_0 (s) ***
$Fe_{50}Pd_{50}$(5%)	$4.2*10^{-11}$
$Fe_{50}Pd_{50}$(10%)	$4.6*10^{-11}$
$Fe_{50}Pd_{50}$(15%)	$9.2*10^{-12}$
$Fe_{50}Pd_{50}$(30%)	$2.1*10^{-13}$

*Assume $\gamma = 0$

Next, the data collapse was performed on the same set of samples at H_0 = 10 Oe with two free parameters, γ and τ_0, using the Eqn. 19 definition of θ^*. The result of this collapse was that several different combinations of γ and τ_0 provided visually similar fits. γ was artificially limited between 0 and 0.2 in order to satisfy the assumptions in [14]. The 20 % sample was dropped from these collapses because of strong interference from the second peak. The results of this collapse are shown in Fig. 11, where each line corresponds to the combinations of γ and τ_0 that provide the best collapse. The color of the line indicates a measure of how complete the data collapse was, with yellow marking the most complete collapse, and blue marking visually similar, but slightly less complete collapses. For example, the 5 % sample was best collapsed by τ_0 values around 5 x 10^{-11} s and γ = 0 while the 30 % sample was best collapsed by γ around 0.2 and τ_0 values around 1 x 10^{-10} s. Therefore, **the decrease in τ_0 seen in Table 3 was attributed to not accounting for the dipolar interaction**. **The values of τ_0 likely stay similar or increase with increasing load.** The main conclusion from this method of data collapse was that while similar particles cause the presence of the first peak, those particles are increasingly influenced by dipolar interactions as the load increased. This analysis provides evidence confirming that **some of the increase in the average blocking temperature as the metallic load increases can be attributed to the dipolar interaction.**

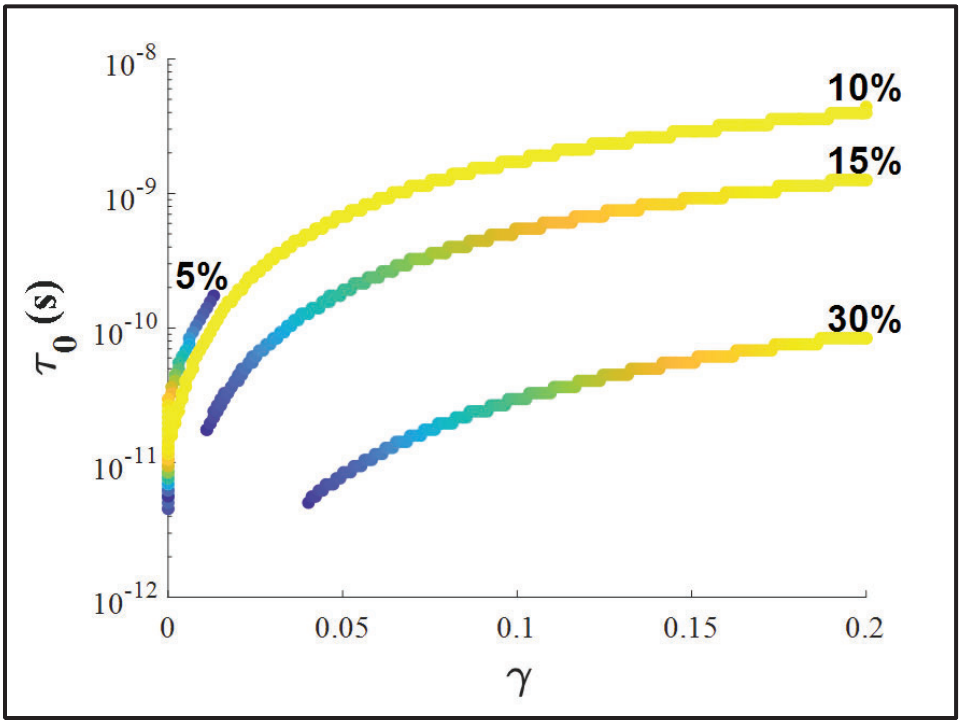

Figure 11: The data in this figure reflect results of data collapses of four $Fe_{50}Pd_{50}$ samples at H_0 = 10 Oe. The Eqn. 19 definition of θ^* was used to collapse the normalized χ'' curves from different frequencies. τ_0 was bounded between 10^{-7} and 10^{-16} while γ was bounded from 0 to 0.2. The lines below indicate the combination of τ_0 and γ which provided visually identical levels of data collapse. All points on the line are from visually similar collapses, but a lighter color indicates a numerically better collapse (i.e. while the $Fe_{50}Pd_{50}$(30%) sample was visually collapsed well by γ = 0.05, it was collapsed increasingly well by increasing γ).

7.4.10. Estimation of magnetic energy barriers for 1st peak for $Fe_{50}Pd_{50}$ nanoparticle biocomposites

The Eqn. 20 model for χ'' curves was applied to data collapses for the simple cases of the 10 % sample at 50 Oe and 100 Oe. A fit was performed using a single distribution of T_B (n = 1). The results of the two fits are shown in Fig. 12. Using the δ_θ calculated in this fit, a value for the energy barrier was approximated using the Arrhenius plot in Fig. 9. The fit indicates that the average height of the energy barrier for the first peak is around 80 ± 15 K in the 10 % sample at 50 and 100 Oe. The values from the Arrhenius plot indicate a slightly higher energy barrier than the values from the data collapse and fitting method. **The average $\boldsymbol{\delta_D}$ of ca. 0.25 indicates that the standard deviation of the diameter of the particles is about 25 % of the diameter of the nanoparticles**. Using the values calculated from the first peak in Table 2, this indicates that the standard deviation of the first peak's particle's diameters is 0.85 nm.

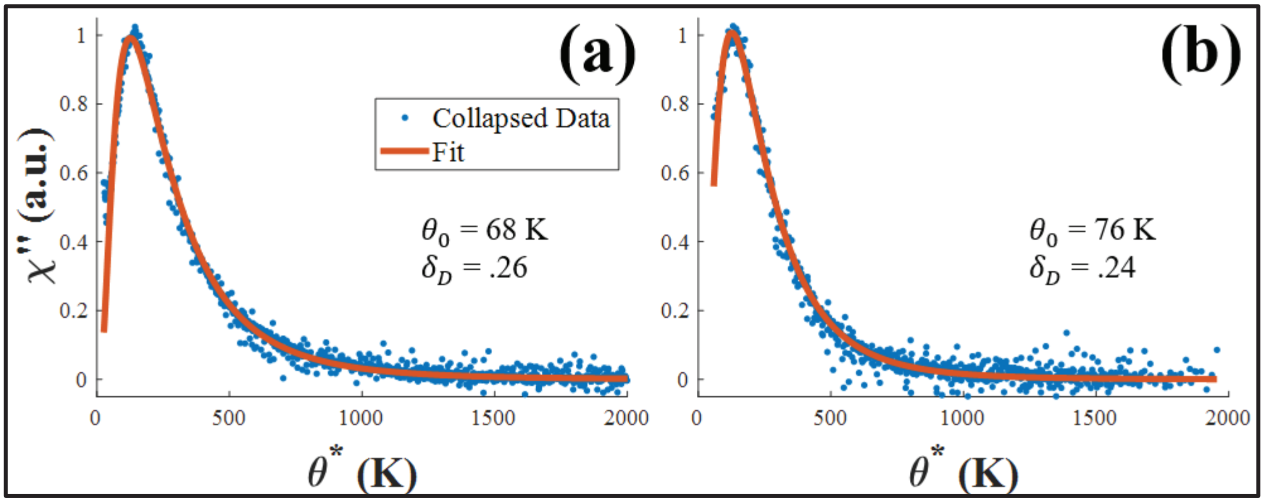

Figure 12: Eqn. 20 fits to normalized, collapsed χ'' data for the $Fe_{50}Pd_{50}$(10%) sample at (a) H_0= 50 Oe and (b) H_0= 100 Oe**.** The data was collapsed with the parameters extracted from the data collapse in Fig. 10. The model of a single particle distribution (n = 1) was used, indicated a single distribution of blocking temperatures. The relevant parameters extracted from this data are annotated within each panel. The data from T = 2 K to 150 K were used in this fit.

In most $Fe_{50}Pd_{50}$ samples, **each peak has a different set of values for $\boldsymbol{\gamma}$ and $\boldsymbol{\tau_0}$**, and therefore one set of γ and τ_0 is unable to collapse the entire dataset. To complicate matters, even when the data collapse is performed on just the first peak, the values of τ_0 and γ are often unable to be determined independently, because most peaks experience interference from one or more neighboring peaks. In order to fit the data using the Eqn. 20 model, it is necessary to a have a set of collapsed data. In order to mitigate these issues, we attempted to isolate and fit just the first peak of the data rather than the whole dataset. An example of fitting just the first peak can be seen in Fig. 13.

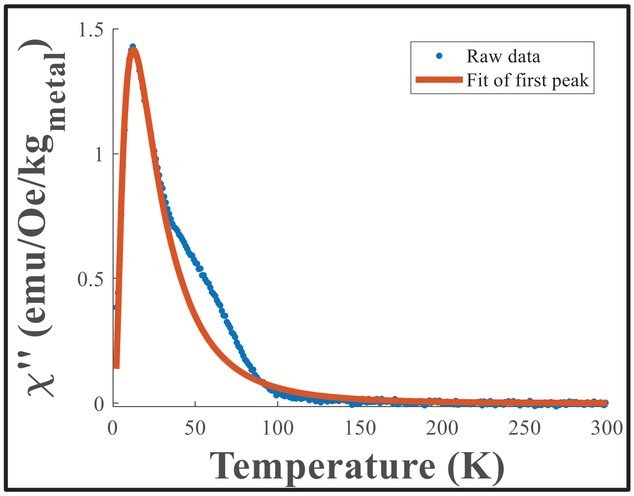

Figure 13: Eqn. 20 fit to the 829 Hz curve of the first peak of the $Fe_{50}Pd_{50}$(10%) sample at H_0= 10 Oe. Only the data from T = 2 to 22 K was used in the data collapse and to fit the curve, although data from T = 2 to 300 K is shown to indicate how the fit covers only the first peak.

However, recall that there were a number of combinations of τ_0 and γ that produced visually similar collapses. Therefore, the fits were performed at a number of combinations of τ_0 and γ. Then, the fitting parameters θ_0 and δ_D were compared across combination of τ_0 and γ. It was determined that while the value of θ_0 depends on γ (and so θ_0 cannot be independently determined), the value of δ_D is constant with γ. Therefore, meaningful values of δ_D are able to be extracted even without fixing τ_0 or γ. The resulting values of δ_D for the **first peak** at varying loads are shown in Table 4. The values of δ_D were calculated separately for H_0 = 10 Oe and H_0 = 50 Oe and then averaged to arrive at the data in Table 4. **The trend of the δ_D clearly indicates that the dispersion of diameters increases with load.** This supports the conclusion that the samples become increasingly heterogenous as the load increases.

Table 4: The following table shows the evolution of the fitting parameter δ_D from Eqn. 20 fits of various Fe-Pd samples. The data from H_0= 10 Oe and H_0= 50 Oe were averaged in order to produce this data. The value of δ_D was fixed between 0.03 and 0.5. The δ_D parameter represents the ratio between the standard deviation and the mean diameter.

Sample	δ_D
$Fe_{50}Pd_{50}$(5%)	0.24
$Fe_{50}Pd_{50}$(10%)	0.26
$Fe_{50}Pd_{50}$(15%)	0.37
$Fe_{50}Pd_{50}$(20%)	0.46
$Fe_{50}Pd_{50}$(30%)	0.50

8. Results and discussion for Fe-Ni nanoparticle biocomposites

8.1. Characterization of the energetic event observed during reduction of Fe-Ni nanoparticle biocomposites

8.1.1. Energetic event observed in Fe-Ni nanoparticle biocomposites reduced at 120 °C

Table 5 summarizes the Fe-Ni samples that were evaluated in this study. All Fe-Ni samples were prepared with a theoretical metal load of 20 wt. %. ATR-FTIR of selected samples reduced at 120 °C, shown in Fig. 14, indicated that IW using Fe and Ni nitrate salts could deliver a composite material for which the underlying support matrix is preserved. The vibrational stretches observed in the IR data for $Fe_{75}Ni_{25}$(20%), $Fe_{50}Ni_{50}$(20%), $Fe_{25}Ni_{75}$(20%), Fe_5Ni_{95}(20%), and Fe_3Ni_{97}(20%) are characteristic of the bonding present in cellulose (i.e., stretches at 3300, 2950, and 1020 cm^{-1} represent O−H, C−H, and C−O, respectively [5]. These results were expected based on prior studies of Pd-based bimetal nanoparticles in cellulose-based supports [6,7].

Table 5: Samples in this table reflect all of the Fe-Ni samples reduced at 120 °C and 200 °C. The parenthetically separated number reflects the number of replicates of the sample. The **bolded** samples underwent an energetic event during the nitrogen reduction.

Reduction Temperature	
120 °C	**200 °C**
Ni_{100} (5)	**Ni_{100} (3)**
Fe_1Ni_{99} (3)	**Fe_5Ni_{95}**
Fe_2Ni_{98}	**$Fe_{10}Ni_{90}$**
Fe_3Ni_{97}	$Fe_{25}Ni_{75}$*
Fe_5Ni_{95}	$Fe_{75}Ni_{25}$
$Fe_{25}Ni_{75}$	
$Fe_{50}Ni_{50}$	
$Fe_{75}Ni_{25}$	
Fe_{100}	

*Partial energetic event observed

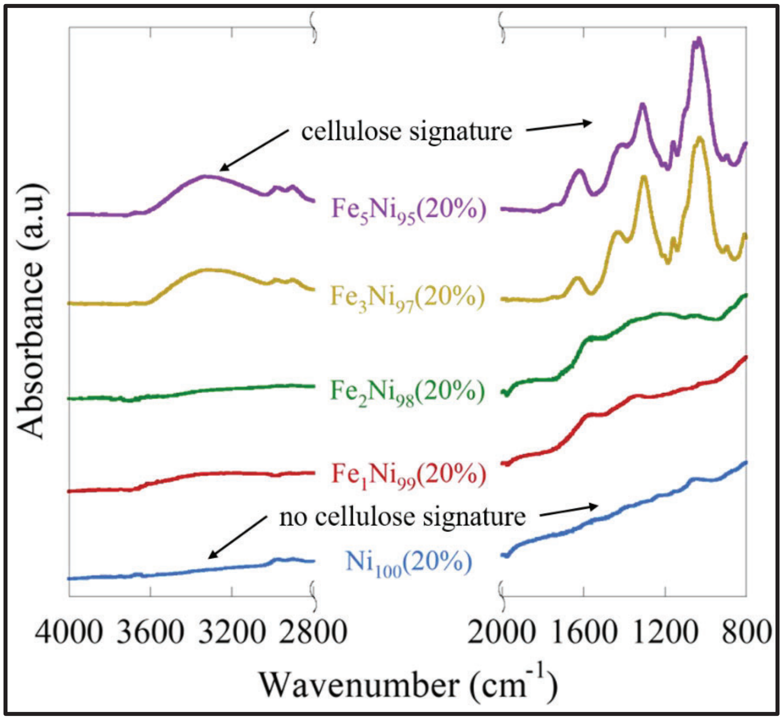

Figure 14: Attenuated total reflectance Fourier transform infrared spectroscopy (ATR-FTIR) of selected Fe-Ni samples reduced at 120 °C. Curves have been shifted vertically for clarity. The peaks typically observed when cellulose is present have been annotated. The absence of those peaks in the low iron-content samples have been annotated.

However, in samples containing Ni for which the Fe content was at or below 2 at. %, a destructive 'energetic event' was routinely observed at 120 °C during the N_2 reduction phase that resulted in the degradation of the cellulose matrix. Each sample for which this energetic event was observed are listed in bold in Table 5. A photo of the tube furnace after the explosion under N_2 in the Ni_{100}(20%) sample is presented in Fig. 15 (b). To contain the sample during each event, the ceramic boat was wrapped in aluminum foil. Video records indicate the energetic event typically occurs after about an hour of exposure to N_2 at 120 °C. During the energetic event, the sample would lose significant mass, change color from green to black, and the signature of functional groups typically seen in cellulose are no longer present in the ATR-FTIR data. SEM investigation of these materials indicates that the event has removed nearly all signs of the fibrous macrostructure typically present in cellulose as seen in Fig. 16 where the samples in panels (a), (b), and (d) experienced energetic events while the sample in (c) did not. The mechanism for the energetic event is currently unknown, but it is hypothesized that nitrocellulose may be formed from the nitrates in the metal salts used in IW. Nitrocellulose is highly flammable and the reduction process at 120 °C is clearly enough to trigger combustion of the material.

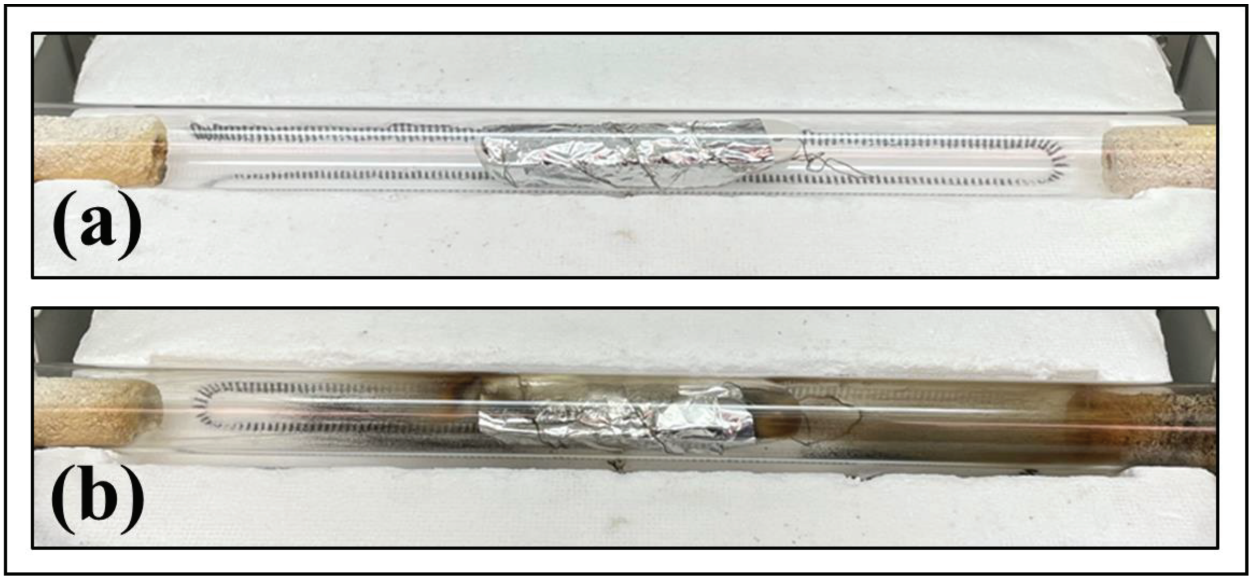

Figure 15: Photographs of a Ni_{100}(20%) sample (a) before and (b) after the energetic event during the nitrogen reduction. The ceramic boat covered in foil in the center of the frame holds the powdered sample. The aluminum foil is "tented" over the boat to reduce the amount of powder flung from boat during the explosion while allowing gas flow to the sample. As can be seen, powder and other products of the explosion can be seen coating the inside of the glass tube despite the foil cover.

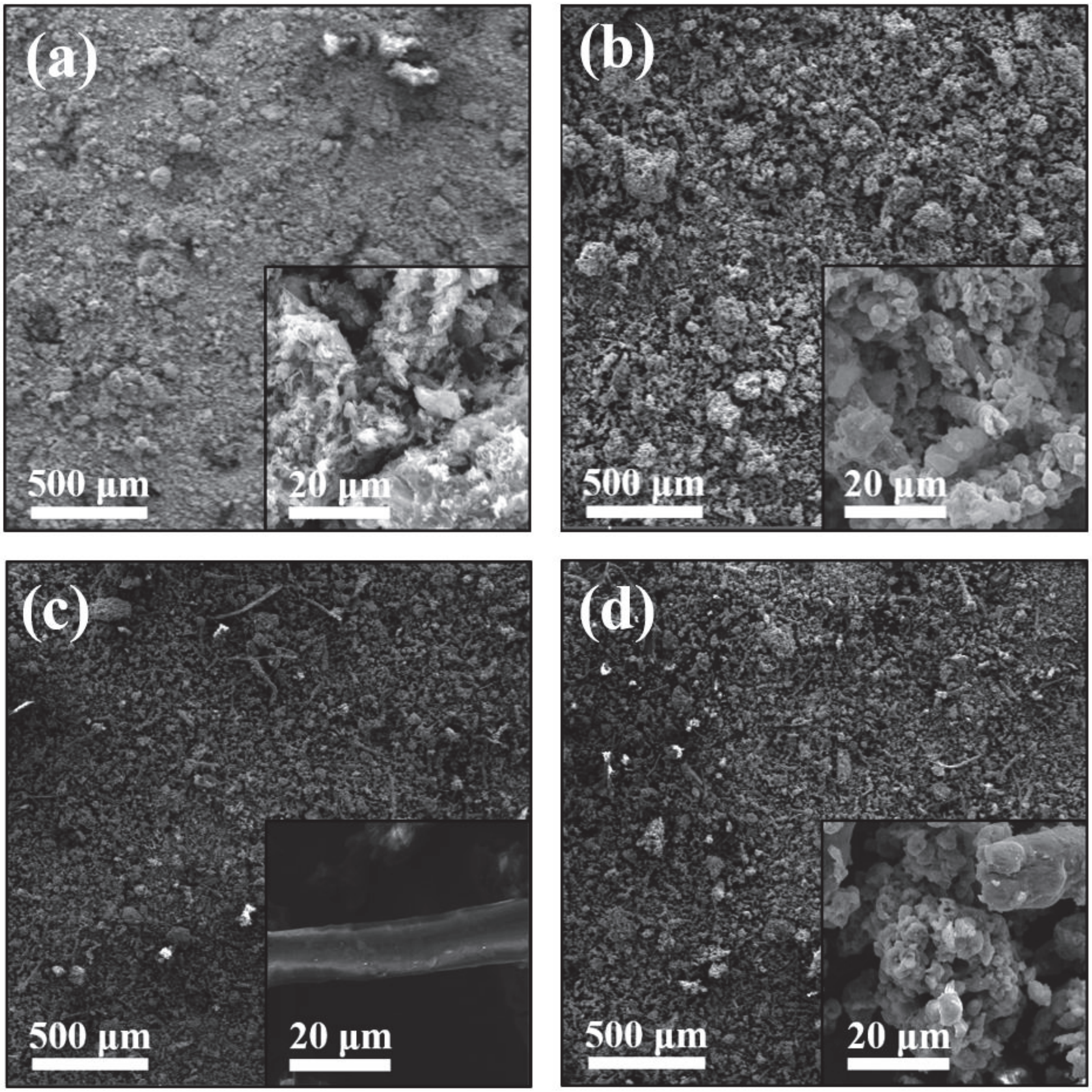

Figure 16: Images generated from scanning electron microscopy (SEM) at two different scales of (a) Ni_{100}-A reduced at 120 °C, (b) Fe_1Ni_{99} reduced at 120 °C, (c) Fe_5Ni_{95} reduced at 120 °C, and (d) Fe_5Ni_{95} reduced at 200 °C. Energetic events were observed during the nitrogen reduction of the Ni_{100}-A in (a), Fe_1Ni_{99} in (b), and Fe_5Ni_{95} in (d). Note that the Fe_1Ni_{99} pictured in (b) experienced an oxidation event after reduction.

In the samples with more than 2 at. % Fe for which the cellulose matrix remains intact, weak magnetization and little evidence of any blocking temperature is observed. This indicates poor nanoparticle formation, which is reflected in TEM data that shows few nanoparticles. On the other hand, in the samples for which the cellulose matrix is destroyed, the amorphous carbon matrix that remains has proved to be a good source of nanoparticles. **TEM data in Fig. 17 shows nanoparticle formation in the Ni_{100}(20%) sample**.

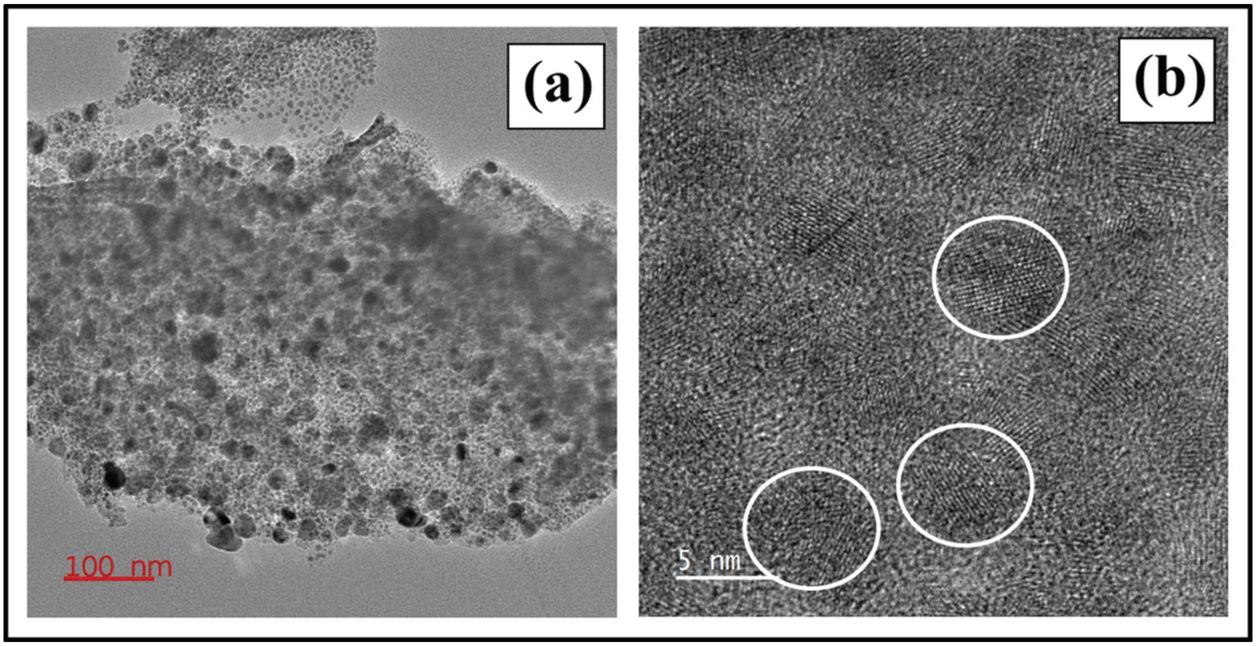

Figure 17: Transmission electron microscopy data (TEM) of Ni_{100}(20%) reduced at 120 °C can be seen at (a) low resolution and (b) high resolution. Three white circles have been annotated in (b) to draw the eye to the lattice fringes indicating nanoparticles.

The clearest indicator for whether an energetic event had occurred was powder XRD measurements. In Fig. 18, a comparison of powder XRD data is shown between the Fe_2Ni_{98}(20%) sample for which an energetic event had occurred and the Fe_5Ni_{95} sample where no energetic event occurred. The peaks seen in the Fe_2Ni_{98}(20%) sample indicate the presence of face centered cubic **(fcc) Ni structure** within the sample. In the Fe_5Ni_{95}(20%) sample for which no energetic event occurred, broad peaks from $2\theta = 10°$ to $30°$ indicate the amorphous structure of the cellulose matrix only, and no peaks are seen that can be definitively attributed to crystalline Ni structure. These data suggest that the energetic event that transformed the cellulose into an amorphous carbon support played a critical role in forming the crystalline Ni and Fe-Ni nanoparticles responsible for their nanomagnetic properties. The XRD profiles from ≥ 5 at. % samples are consistent with XRD from Fe-Pd samples for which no energetic event occurred.

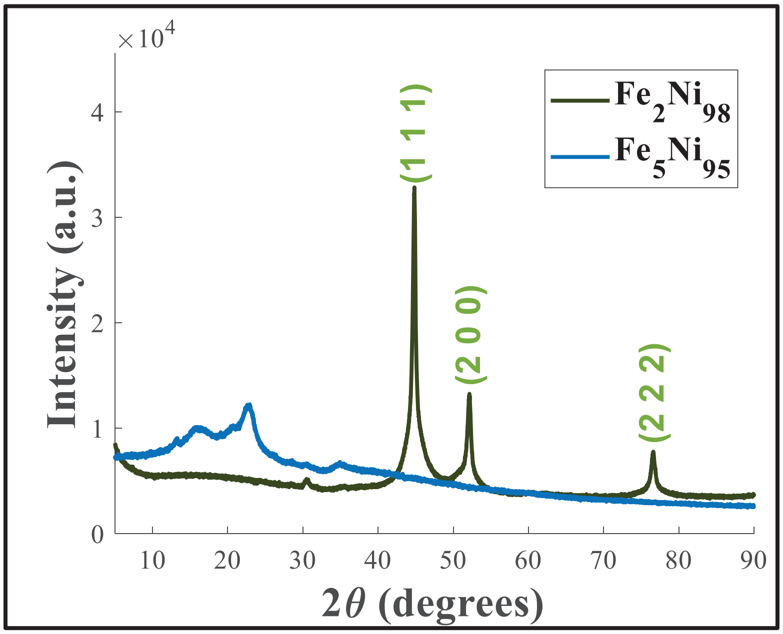

Figure 18: XRD data from a sample for which an energetic event was observed (Fe_2Ni_{98}) and for which no energetic event was observed (Fe_5Ni_{95}). Both samples were reduced at 120 °C. The XRD data were measured at 35 kV/30 mA and averaged over 30 scans. The fcc Ni peaks are annotated.

In addition to the presence of fcc Ni peaks correlating to the observation of an energetic event, the height of the Ni peaks was found to be proportional to the room temperature magnetization of Fe-Ni samples. This trend can be seen in Fig. 19. Increased peak height and sharpness are generally correlated with increased grain size. The positive correlation between room temperature magnetization and XRD peak height is attributed to increasing particle size.

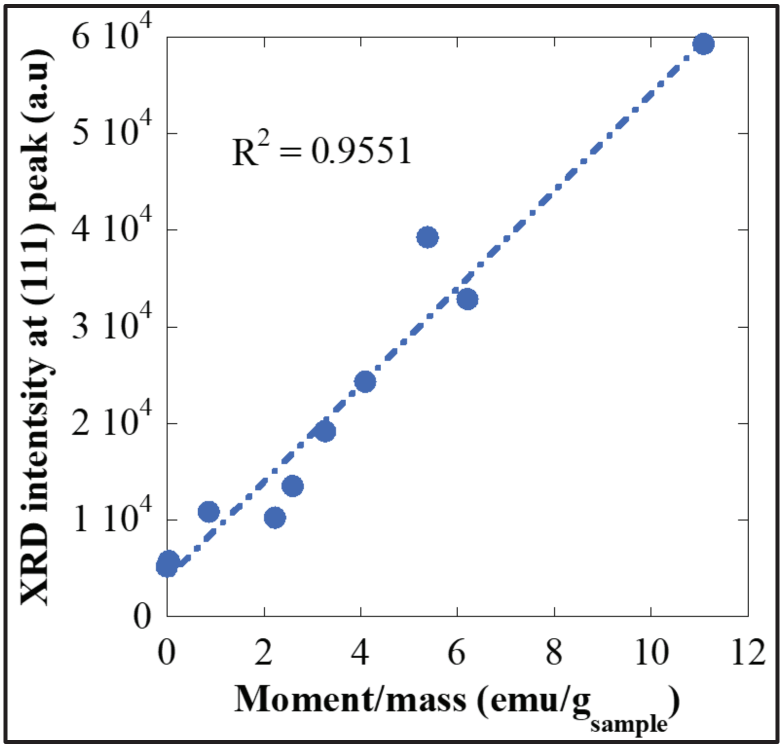

Figure 19: The data shown reflect the correlation seen between the intensity of the (111) Ni peak in XRD scans and normalized magnetic moment at 300 K of various Fe-Ni samples reduced at 120 °C and 200 °C.

8.1.2. Energetic event observed in Fe-Ni samples reduced at 200 °C

After determining that the energetic event was a necessary condition for the formation of nanoparticles in the Fe-Ni nanoparticle biocomposites, the temperature of reduction was increased in order to probe whether the energetic event could be observed at higher iron-concentrations. As reflected in the bolded samples in Table 5, the threshold for an energetic event was pushed to a higher iron-concentration, for which energetic events were observed during the 200 °C N_2 reduction at 5 and 10 at. % Fe. The energetic event for these samples occurred shortly after the start of the nitrogen reduction. A partial energetic event, shown in the Fig. 20, occurred in the $Fe_{25}Ni_{75}$ sample at 200 °C. Therefore, the threshold for a complete energetic event for Fe-Ni in cellulose is likely around 20 at. % Fe when total metal loading is 20 wt. %.

Figure 20: A photograph of the $Fe_{25}Ni_{75}$(20%) boat was taken shortly after reduction at 200 °C. The brown color seen across the majority of the sample is typical of no energetic event. The small blackened area in the middle of the boat is more typical of the powder resulting from an energetic event. Therefore, this composition was classified as a “partial” energetic event.

8.2. Characterization of the oxidation event observed after reduction of Fe-Ni nanoparticle biocomposites

In some of the samples for which an energetic event occurred during the N_2 phase of reduction, there was a second combustion event that occurred after completing the H_2 phase of the reduction. After the H_2 gas was purged from the tube furnace by N_2 gas, the sample ignited upon removal from the tube furnace, and a slow burn process caused further mass loss. This oxidation event is attributed to an unusually high amount of hydride stored in the Ni-Fe nanoparticle matrix after the hydrogen reduction, which ignited upon release, recombination, and exposure to atmospheric oxygen. The event occurred in three different samples: Fe_1Ni_{99}(20%) after a 120 °C reduction, Ni_{100}(20%) after a 200 °C reduction, and a separate Ni_{100} sample regenerated at 120 °C after being reduced at 200 °C a few days earlier. Originally, a 10-minute purge under N_2 gas was employed. After the first such event, the 10-minute purge was lengthened to 20 minutes. After the second event, the 20-minute purge was lengthened to 120 minutes. After the third oxidation event, the purge was lengthened to 12 hours. No sample has ignited after a 12-hour purge.

XRD data for a Ni_{100}(20%) sample reduced at 200 °C, shown in Fig. 21, demonstrate the effect of the oxidation event on the structure of the material. Before the oxidation event, only fcc Ni peaks are present. The sample was regenerated at 105 °C and an oxidation event occurred after a two-hour purge. **After the oxidation event, fcc Ni and fcc NiO peaks are visible**. The presence of fcc NiO suggests that the Ni and Ni-Fe nanoparticle matrices act like a **nickel-hydride battery** that holds onto hydrogen during the N_2 purge and reacts with oxygen, causing ignition of the remaining hydrocarbons in the sample upon exposure to the atmosphere. Further experiments evaluating the adsorption properties of these systems (i.e., chemisorption) are necessary in order to understand the extent that hydride is being stored and/or released from the nanoparticles.

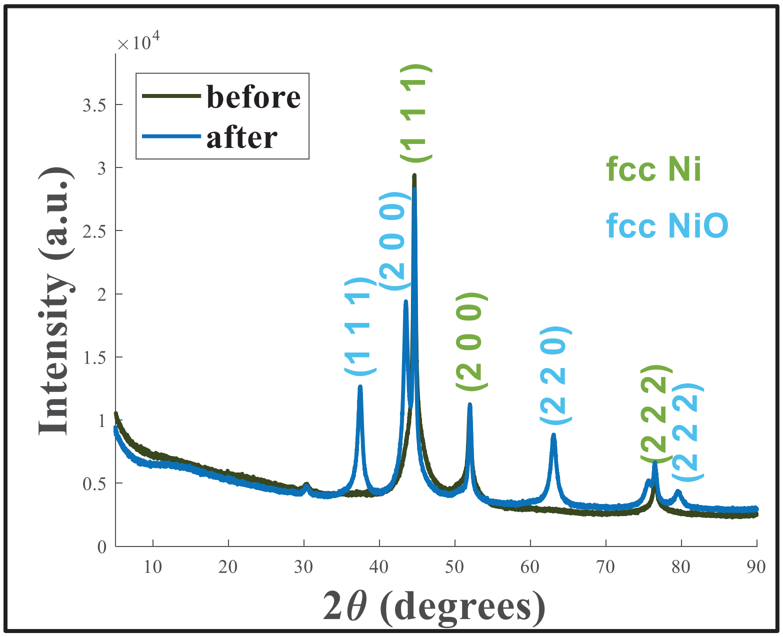

Figure 21: XRD data from the same Ni_{100}(20%) before and after the oxidation event. The Ni_{100} sample was first reduced at 200 °C. Then, the sample was regenerated at 105 °C. Oxidation was observed after a two-hour nitrogen purge. The XRD data were measured at 35 kV/30 mA and averaged over 30 scans. The fcc Ni and fcc NiO peaks are annotated.

8.3. Reproducibility issues within the synthesis of the series of Fe-Ni nanoparticle biocomposites reduced at 120 °C

The reproducibility of the Ni_{100}(20%) synthesis and corresponding energetic event at 120 °C was probed by reducing five identical Ni_{100}(20%) samples (labeled as -A, -B, -C, etc.) at 120 °C. Comparison of XRD scans was used in order to determine the degree of reproducibility. To probe the stability of the XRD profiles of the Fe-Ni samples, XRD measurements were performed on the same sample multiple times at the interval of one hour, one day, and three days. All scans were identical, giving confidence that the XRD profiles of each sample would remain relatively constant over this time period. Even though this gave a reasonable degree of confidence in the stability of XRD profiles, a consistent procedure of taking XRD measurements within a day of reduction was employed. The XRD data of all five Ni_{100}(20%) samples reduced at 120 °C can be seen in Fig. 22. The first Ni_{100}(20%) sample (Ni_{100}-A), exhibits a vastly different XRD profile from the B-E samples. Flame AAS data, shown in Table 6, indicate that there was a significant difference in the total metal load between the Ni_{100}-A and Ni_{100}-B samples. Magnetic ZFC measurements of Ni_{100}-A and Ni_{100}-B in Fig. 23 show that the difference in structure seen in XRD is also reflected in different magnetic properties. These measurements suggest that the Ni_{100}-A had a more complete energetic event, causing increased agglomeration and a greater load. The larger nickel particles likely have a larger domain size and a higher degree of magnetic order, causing the larger, sharper peaks in the XRD profile. This is also corroborated by the peak in ZFC magnetization around 300 K which likely corresponds to large nickel particles. There is evidence of a lower temperature peak, seen around 20 K, in both samples. This peak likely corresponds to the T_B of the nanoparticles present in the sample. The different character of the energetic events can also be visually observed in Fig. 24, which shows the tube furnace after the energetic events in the Ni_{100}-A and Ni_{100}-B samples.

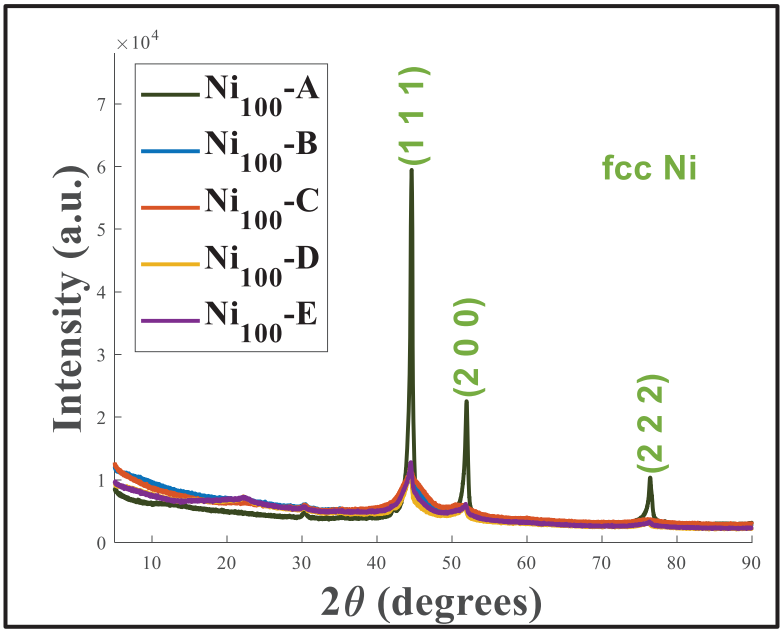

Figure 22: XRD data of five Ni_{100} (20%) samples reduced at 120 °C. The -A, -B, etc. indicates a replicate of Ni_{100}. The fcc Ni peaks are annotated. The XRD data were measured at 35 kV/30 mA and averaged over 30 scans.

Table 6: The data in this table represent the results of Flame AAS analysis of various Fe-Ni samples. Bolded samples underwent an energetic event. The Fe_1Ni_{99}(20%) sample underwent an oxidation event.

Sample	Reduction Temperature (°C)	Fe (Mass %)	Ni (Mass %)	Total Mass Metal (%)	Atomic % (Fe/(Ni+Fe))
Ni_{100}(20%)-A	120	0.0	76.0	76.0	0.0
Ni_{100}(20%)-B	120	0.0	38.5	38.5	0.0
Fe_1Ni_{99}(20%)	120	0.7	75.2	76.0	1.0
Fe_2Ni_{98}(20%)	120	1.2	57.6	58.7	2.1
Fe_3Ni_{97}(20%)	120	0.5	14.6	15.1	3.5
Fe_5Ni_{95}(20%)	120	0.8	14.3	15.1	5.6
Ni_{100}(20%)	200	0.0	56.2	56.2	0.0
Fe_5Ni_{95}(20%)	200	2.6	52.7	55.3	5.3
$Fe_{10}Ni_{90}$(20%)	200	4.6	43.8	48.5	11.1

*Note: Flame AAS measurements reflect analysis of samples in triplicate, with RSD of 0.5% in absorbance values. Sample labels reflect theoretical loading of Fe and Ni with respect to each other in atomic percentage and total metal loading in mass percentage with respect to the total matrix (i.e., Fe_1Ni_{99}(20%) was targeted as 1 at % Fe and 99 at % Ni in cotton fiber at total metal loading of 20 mass %). The samples measured by Flame AA were representative powders of the same batches analyzed in the PPMS.

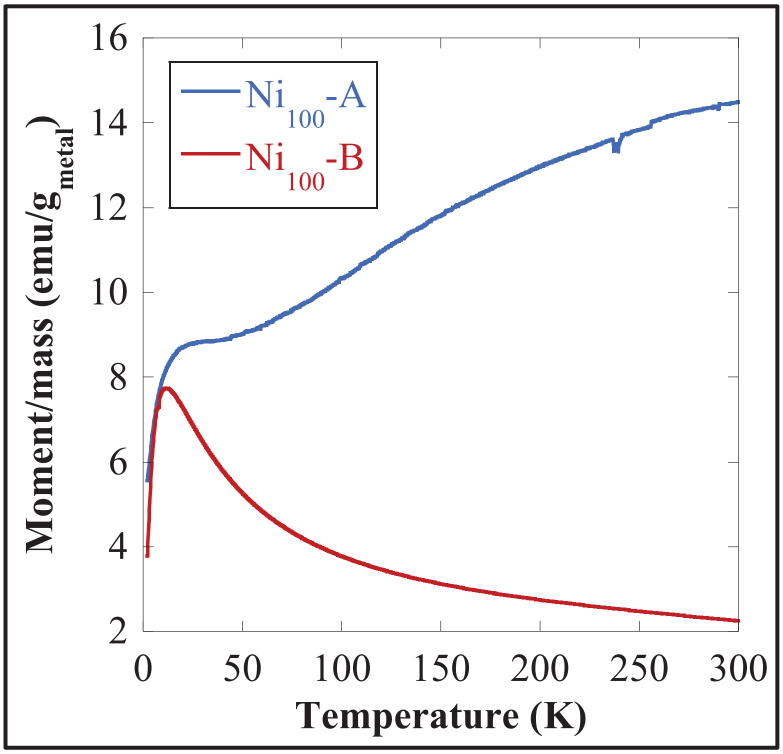

Figure 23: Zero-field-cooled (ZFC) magnetization curves of the first and second Ni$_{100}$ samples reduced at 120 °C. Magnetization was measured from 2 K to 300 K under a static 250 Oe field. The magnetic moment has been normalized to the combined mass of Ni in the sample using the compositions calculated from AAS measurements.

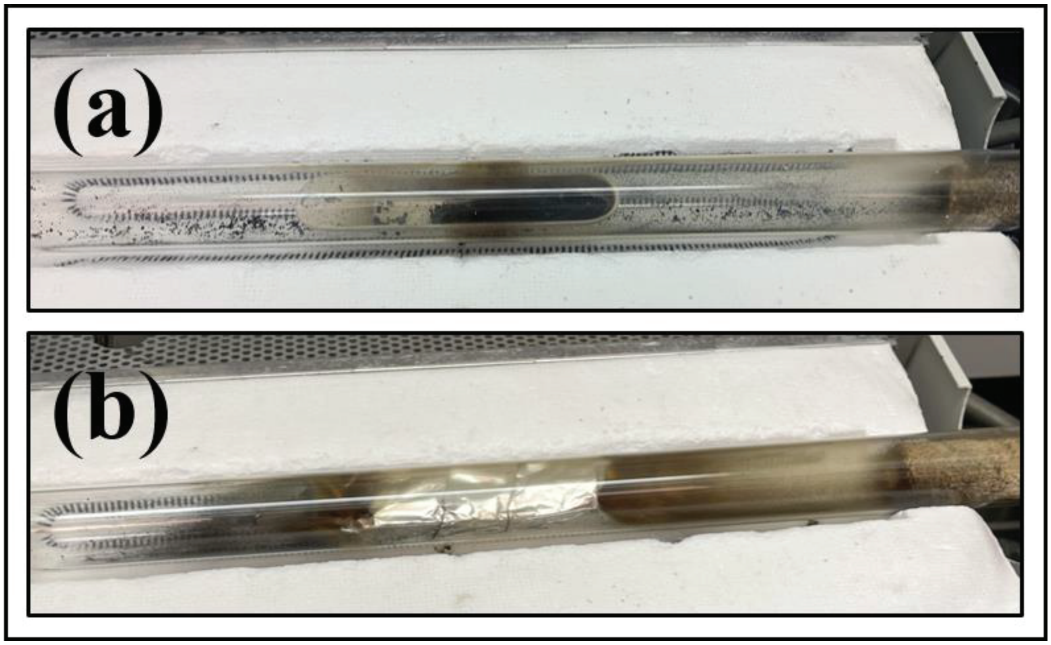

Figure 24: Photographs of the (a) Ni$_{100}$-A sample and (b) Ni$_{100}$-B sample after experiencing an energetic event during N_2 reduction.

In order to try and replicate the first Ni_{100}-A event, experimental parameters were tweaked in the each of the subsequent samples (Ni_{100}-C, -D, and -E). The flow rate of N_2 gas was doubled, the sample was placed in the tube furnace with and without an aluminum “tent” to retain sample thrown about by the energetic event (Note: Ni_{100}-A was the first sample produced in this study and reduce while “untented”), and XRD was measured before and after regeneration at 105 °C. In every case, the subsequent four samples (Ni_{100}-B, -C, -D, and -E) displayed a remarkably similar XRD profile. Therefore, the mechanism causing the different nature of the energetic event in the Ni_{100}-A sample is still unknown. Regardless of what caused the Ni_{100}-A sample to develop different characteristics, the subsequent samples were generally very reproducible.

8.4. Magnetic analysis of low-Fe content Fe-Ni nanoparticle biocomposites

The normalized ZFC and FC magnetization curves of Fe-Ni samples reduced at 120 °C are presented in Fig. 25 (a) and the Fe-Ni samples reduced at 200 °C can be seen in Fig. 25 (b). **From the data, it is clear that the energetic event is required for creating a nanoparticle biocomposite with a strong magnetic response.** In samples with no energetic event, there is limited evidence of a blocking temperature and the magnitude of magnetization is orders of magnitude lower. An oxidation event was observed for Fe_1Ni_{99}(20%) reduced at 120 °C. The oxidation event appears to have reduced the room temperature magnetization as the Ni became oxidized to NiO, which has a lower saturation magnetization than zero-valent Ni. Furthermore, there is reason to believe that the oxidation event may have caused the agglomeration of nanoparticles into much larger particles, since there is little evidence of a low temperature T_B.

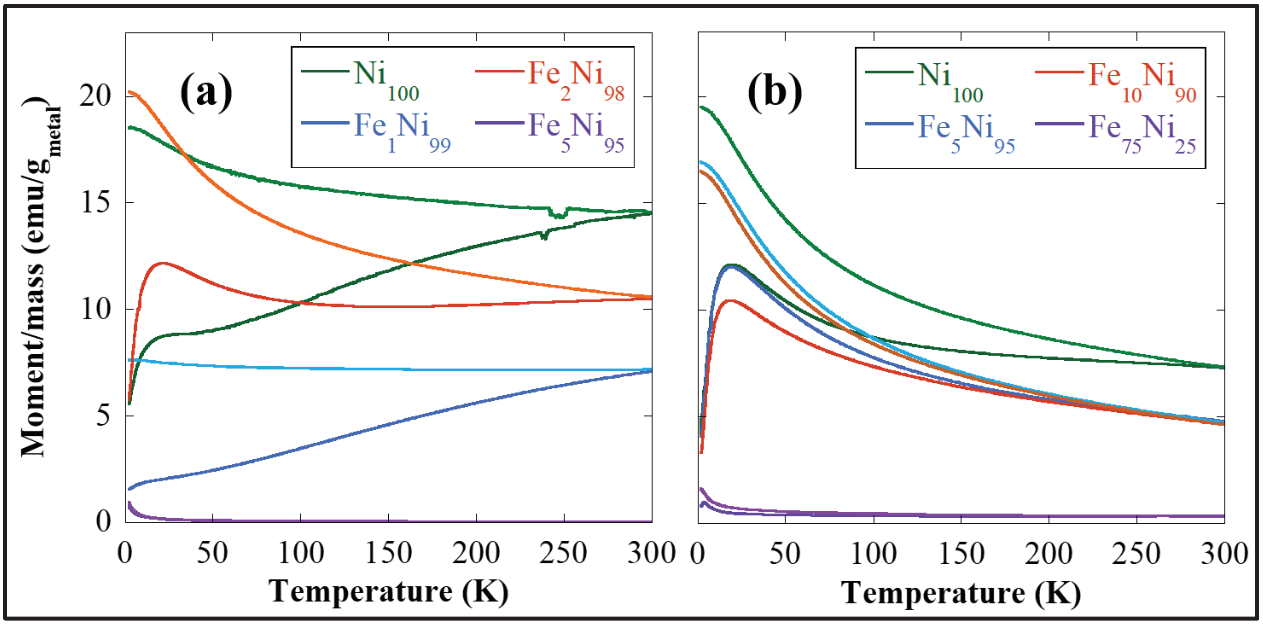

Figure 25: ZFC and FC magnetization curves of the Fe-Ni series reduced at 120 °C in (a) and reduced at 200 °C in (b). Magnetization was measured from 2 K to 300 K under a static 250 Oe field. The magnetic moment has been normalized to the combined mass of Fe and Ni in the sample using the compositions calculated from AAS measurements. Note that the Fe_1Ni_{99} sample in (a) experienced an oxidation event. Every sample except the Fe_5Ni_{95} reduced at 120 °C and the $Fe_{75}Ni_{25}$ reduced at 200 °C experienced energetic events.

In all other samples that experienced an energetic event, there is evidence of a T_B around 20 K. Due to reproducibility issues within the synthesis of Fe-Ni composites at 120 °C, it is difficult to draw any conclusions for samples reduced at that temperature beyond that the fact that there are nanoparticles present. In contrast, the 200 °C series appears to show increased reproducibility based on the consistent ZFC/FC magnetization data, AAS metal loads, XRD measurements, and visual observations of the tube after the energetic event. This difference is attributed to the energetic event being triggered more reliably at 200 °C. Observations of the 120 °C series indicates the energetic event occurs an hour or more into the nitrogen reduction whereas the event occurs only minutes into the 200 °C reduction. Therefore, it is hypothesized that the energy barrier needed to start the energetic event is more easily overcome at a higher temperature.

In the 200 °C series shown in Fig. 25 (b), there appears to be little change in the T_B and T_{irr} as the atomic composition changes. In order to make more detailed comparisons between the T_B of the four samples, AC magnetic susceptibility measurements will likely be needed. However, the magnitude of magnetization does tend to decrease with increasing iron content. XRD data in Fig. 26 suggest a similar trend of **decreasing magnetic response with increasing iron content**. The (111) peak height clearly decreases with increasing iron content. XRD measurements are more sensitive to the size of the magnetic domain, so it is hypothesized that introduction of iron into the nickel matrix may lead to the **iron frustrating the nickel spins**, leading to the decrease of the size of the magnetic domain. Hence, the magnetic response decreases as the domain size decreases. TEM and AC magnetic susceptibility measurements are likely needed in order to fully understand the magnetic response of these biocomposites.

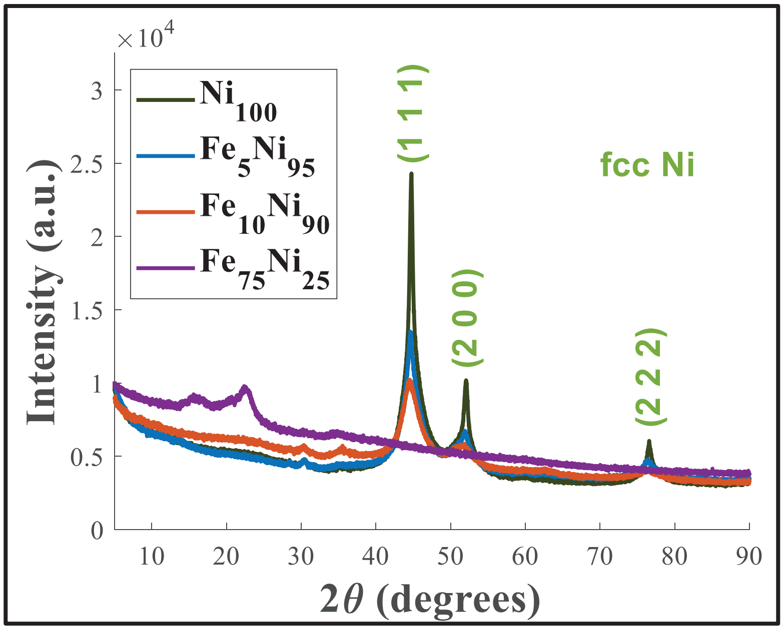

Figure 26: XRD data of Fe-Ni samples reduced at 200 °C. The fcc Ni peaks are annotated. The XRD data were measured at 35 kV/30 mA and averaged over 30 scans.

9. Conclusions

9.1. Conclusions from the study of $Fe_{50}Pd_{50}$ nanoparticle biocomposites

As the total metal loading increases in $Fe_{50}Pd_{50}$ biocomposites, monotonically increasing T_B, T_{irr}, and magnitude of magnetization are observed from the FC and ZFC magnetization curves. These features indicate an increase in the energy barrier to flip the magnetic moment, but provide limited insight into the distribution of magnetic nanoparticles present in the material. AC magnetic susceptibility studies reveal a more nuanced view of the effects of increasing the metal load. The χ' curves confirm the hypothesis that the magnitude of magnetization and average energy barrier increases with temperature. **The χ'' curves indicate up to four distributions of T_B are present**. As the load increases, the higher energy distributions of T_B emerge. Coupled with evidence of agglomeration from previous studies [1], this increase in T_B is partly attributed to either **increased average particle size or clustering**. Analysis of relaxation times of the first peak indicate that there is also an increase in contributions from **dipolar interactions**.

The results of this investigation can be used to inform the production of future systems that incorporate Fe-Pd nanoparticle biocomposites. Moreover, the results also give generalized insight into the effects of altering the metal load in similar bimetallic cellulose-based systems. Because the cellulose matrix is still intact, post-production methods that exploit the properties of the biopolymer can be employed to incorporate the Fe-Pd nanoparticle biocomposite powders into materials ready for application.

9.2. Conclusions from the study of Fe-Ni nanoparticle biocomposites

This report presents the first inquiry into a novel Fe-Ni nanoparticle biocomposite system. A reproducible energetic event during the N_2 reduction process has been observed in 20 wt. % metal biocomposites with ≤ 2 at. % Fe (with respect to Ni) reduced at 120 °C. When reduced at 200 °C, this threshold is extended to ca. 20 at. % Fe. An energetic event of this nature has not been observed before in any of the previously synthesized nanoparticle biocomposite systems. The mechanism for the event is still unknown. The event degrades the cellulose matrix and produces a **magnetically active ensemble of nanoparticles**. Samples without an energetic event do not display comparable magnetic properties or consistent nanoparticle formation. The reproducibility of the event was probed with a combination of powder XRD, Flame AAS, and magnetic measurements. While the 120 °C was generally reproducible, there were several outliers. Samples reduced at 200 °C were consistently reproducible. Magnetization and XRD data from the 200 °C series suggest that the introduction of iron into the nickel matrix may lead to frustration of nickel spins and a decrease in the magnetic response. Future work will be dedicated to the detailed analysis of the effects of introducing iron into the nickel matrix.

A unique event was observed several times in which the sample ignited upon atmospheric exposure. This led to oxidation of the fcc Ni nanoparticle distribution resulting in the introduction of an fcc NiO phase in XRD data. This was attributed to excess hydride stored in the Ni and Ni-metal nanoparticle matrices, akin to Ni-hydride batteries. While the degradation of the cellulose matrix limits the biocomposite from being using post-production methods that rely on the cellulose structure, the nanoparticle matrix can still be readily applied as an electromagnetic shield by combining the powdered biocomposite with a polymer such as poly(ethylene oxide).

10. References

[1] H. Shokrollahi, A. Khorramdin, and Gh. Isapour, *Magnetic Resonance Imaging by Using Nano-Magnetic Particles*, Journal of Magnetism and Magnetic Materials **369**, 176 (2014).

[2] S. Singamaneni, V. N. Bliznyuk, C. Binek, and E. Y. Tsymbal, *Magnetic Nanoparticles: Recent Advances in Synthesis, Self-Assembly and Applications*, Journal of Materials Chemistry **21**, 16819 (2011).

[3] A. G. Kolhatkar, A. C. Jamison, D. Litvinov, R. C. Willson, and T. R. Lee, *Tuning the Magnetic Properties of Nanoparticles*, International Journal of Molecular Sciences.

[4] V. L. Calero-Diaz Del Castillo and C. Rinaldi, *Effect of Sample Concentration on the Determination of the Anisotropy Constant of Magnetic Nanoparticles*, IEEE Transactions on Magnetics **46**, 852 (2010).

[5] D. P. Durkin, T. Ye, E. G. Larson, L. M. Haverhals, K. J. T. Livi, H. C. de Long, P. C. Trulove, D. H. Fairbrother, and D. Shuai, *Lignocellulose Fiber- and Welded Fiber-Supports for Palladium-Based Catalytic Hydrogenation: A Natural Fiber Welding Application for Water Treatment*, ACS Sustainable Chemistry and Engineering **4**, 5511 (2016).

[6] D. P. Durkin, T. Ye, J. Choi, K. J. T. Livi, H. C. D. Long, P. C. Trulove, D. H. Fairbrother, L. M. Haverhals, and D. Shuai, *Sustainable and Scalable Natural Fiber Welded Palladium-Indium Catalysts for Nitrate Reduction*, Applied Catalysis B: Environmental **221**, 290 (2018).

[7] A. Aiello, J. R. Morey, K. J. T. Livi, H. C. DeLong, H. ElBidweihy, P. C. Trulove, and D. P. Durkin, *Lignocellulose-Stabilized Iron-Palladium Nanomagnetic Biocomposites*, Journal of Magnetism and Magnetic Materials **497**, 165964 (2020).

[8] B. Wicklein, A. Kocjan, G. Salazar-Alvarez, F. Carosio, G. Camino, M. Antonietti, and L. Bergström, *Thermally Insulating and Fire-Retardant Lightweight Anisotropic Foams Based on Nanocellulose and Graphene Oxide*, Nature Nanotechnology **10**, 277 (2015).

[9] Z. Zeng, T. Wu, D. Han, Q. Ren, G. Siqueira, and G. Nyström, *Ultralight, Flexible, and Biomimetic Nanocellulose/Silver Nanowire Aerogels for Electromagnetic Interference Shielding*, ACS Nano **14**, 2927 (2020).

[10] K. S. Dijith, R. Aiswarya, M. Praveen, S. Pillai, and K. P. Surendran, *Polyol Derived Ni and NiFe Alloys for Effective Shielding of Electromagnetic Interference*, Materials Chemistry Frontiers **2**, 1829 (2018).

[11] K. L. Livesey, S. Ruta, N. R. Anderson, D. Baldomir, R. W. Chantrell, and D. Serantes, *Beyond the Blocking Model to Fit Nanoparticle ZFC/FC Magnetisation Curves*, Scientific Reports **8**, (2018).

[12] D. A. Balaev, S. V. Semenov, A. A. Dubrovskiy, S. S. Yakushkin, V. L. Kirillov, and O. N. Martyanov, *Superparamagnetic Blocking of an Ensemble of Magnetite Nanoparticles upon Interparticle Interactions*, Journal of Magnetism and Magnetic Materials **440**, 199 (2017).

[13] I. J. Bruvera, P. Mendoza Zélis, M. Pilar Calatayud, G. F. Goya, and F. H. Sánchez, *Determination of the Blocking Temperature of Magnetic Nanoparticles: The Good, the Bad, and the Ugly*, Journal of Applied Physics **118**, (2015).

[14] G. T. Landi, F. R. Arantes, D. R. Cornejo, A. F. Bakuzis, I. Andreu, and E. Natividad, *AC Susceptibility as a Tool to Probe the Dipolar Interaction in Magnetic Nanoparticles*, Journal of Magnetism and Magnetic Materials **421**, 138 (2017).

[15] G. Barrera, P. Tiberto, P. Allia, B. Bonelli, S. Esposito, A. Marocco, M. Pansini, and Y. Leterrier, *Magnetic Properties of Nanocomposites*, Applied Sciences (Switzerland) **9**, (2019).

[16] T. Jonsson, J. Mattsson, P. Nordblad, and P. Svedlindh, *Energy Barrier Distribution of a Noninteracting Nano-Sized Magnetic Particle System*, Journal of Magnetism and Magnetic Materials **168**, 269 (1997).

[17] E. B. Peixoto, M. H. Carvalho, C. T. Meneses, V. H. V. Sarmento, A. A. Coelho, B. Zucolotto, and J. G. S. Duque, *Analysis of Zero Field and Field Cooled Magnetization Curves of CoFe2O4 Nanoparticles with a T-Dependence on the Saturation Magnetization*, Journal of Alloys and Compounds **721**, 525 (2017).

[18] K. Nadeem, H. Krenn, T. Traussnig, R. Würschum, D. V. Szabó, and I. Letofsky-Papst, *Effect of Dipolar and Exchange Interactions on Magnetic Blocking of Maghemite Nanoparticles*, Journal of Magnetism and Magnetic Materials **323**, 1998 (2011).

[19] Quantum Design, *Using PPMS Superconducting Magnets at Low Fields*, 1 (2009).

[20] M. Suzuki and I. Suzuki, *Lecture Note on Solid State Physics AC Magnetic Susceptibility*, (2009).

[21] M. Bałanda, *AC Susceptibility Studies of Phase Transitions and Magnetic Relaxation: Conventional, Molecular and Low-Dimensional Magnets*, Acta Physica Polonica A **124**, 964 (2013).

[22] D. Serantes and D. Baldomir, Superparamagnetism and Monte Carlo Simulations, 2012.

[23] J. L. Dormann, D. Fiorani, and E. Tronc, *On the Models for Interparticle Interactions in Nanoparticle Assemblies: Comparison with Experimental Results*, Journal of Magnetism and Magnetic Materials **202**, 251 (1999).

[24] G. F. Goya and M. P. Morales, Field Dependence of Blocking Temperature in Magnetite Nanoparticles, 2004.

[25] C. Tannous and J. Gieraltowski, *The Stoner–Wohlfarth Model of Ferromagnetism*, European Journal of Physics **29**, 475 (2008).

[26] J. Dieckhoff, D. Eberbeck, M. Schilling, and F. Ludwig, *Magnetic-Field Dependence of Brownian and Néel Relaxation Times*, Journal of Applied Physics **119**, (2016).